(p,n) REACTIONS ON ^{59}Co
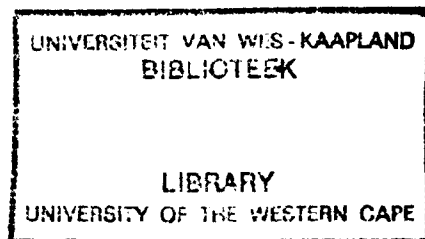# IN THE INTERMEDIATE ENERGY RANGE.

Peter James Bester

A thesis submitted to the Faculty of Science
of the University of the Western Cape in
partial fulfilment of the requirements
for the M.Sc. degree in Physics.

Department of Physics, University of the Western Cape

September 1992

to my mom and dad

Acknowledgements

A great many people and organizations contributed to the presentation of this thesis.
I would like to express my sincere appreciation to the following people:

Contents

List of Figures

List of Tables

Chapter 1

INTRODUCTION

Detailed theoretical investigations [Chi80,Mos82,Kle85] of (p,n) and (p,p′) data indicate that the reaction mechanisms operative at intermediate energies and for energy losses up to several tens of MeV are predominantly single-step in nature. In these direct reactions, only a few nucleons take part in the reaction, with the remaining nucleons of the target serving as passive spectators. Many excited states of the product nucleus can be reached in these reactions.

The charge-exchange nucleon-nucleus reaction at intermediate energies has an unique advantage over other types of reactions, since it has been established [Love81,Love85] that at these energies they preferentially excite nuclear spin-isospin modes. In a single scattering picture, this means that the charge-exchange process is mediated primarily by the spin-isospin part of the effective nucleon-nucleon ($\mathcal{NN}$) interaction. The interaction based on the $\mathcal{NN}$ t- matrix provides a good description of experimental cross sections for those isovector spin-flip excitations for which the relevant aspects of nuclear structure are known [Com82].

The main reasons for the present study was to measure the strength of the
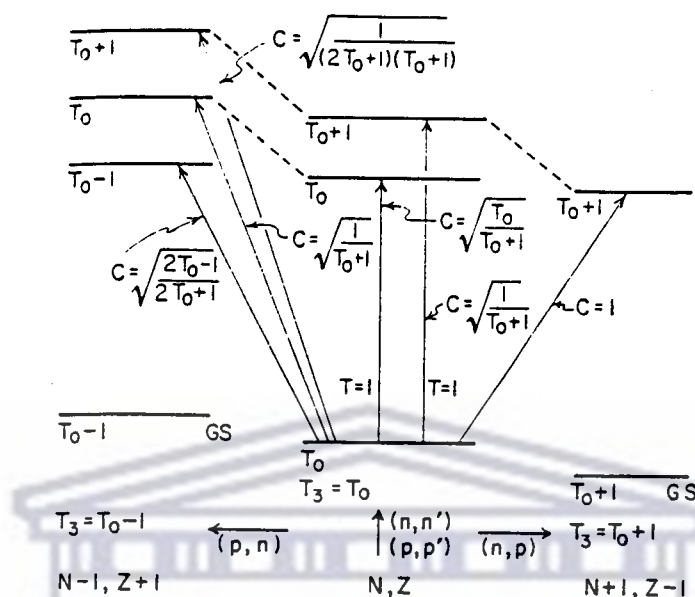
Figure 1.1: *Isovector excitations and isospin vector coupling coefficients, C.*

Gamow-Teller transition and to test the 3(N-Z) sum rule in an odd-mass nucleus.

Previous charge-exchange measurements on odd-mass nuclei has revealed rather large, unexpected differences in their unit cross sections, $\hat{\sigma}(GT)$, compared to those of neighboring even-mass nuclei. These $\hat{\sigma}(GT)$ values were determined from the Gamow-Teller to Fermi (GT/F) strength ratios. The origin of these differences is still unknown, but it might lie in the effective $\mathcal{NN}$ interaction [Love85], or in nuclear structure effects, or in an interplay of both. Fluctuations in $\hat{\sigma}(GT)$ also occur. For example, the $\hat{\sigma}(GT)$ values for ^{13}C, ^{15}N and ^{39}K are larger than those for adjacent nuclei by 40% $\sim$ 50% while the ^{19}F case appears to have 'normal' $\hat{\sigma}(GT)$ values.
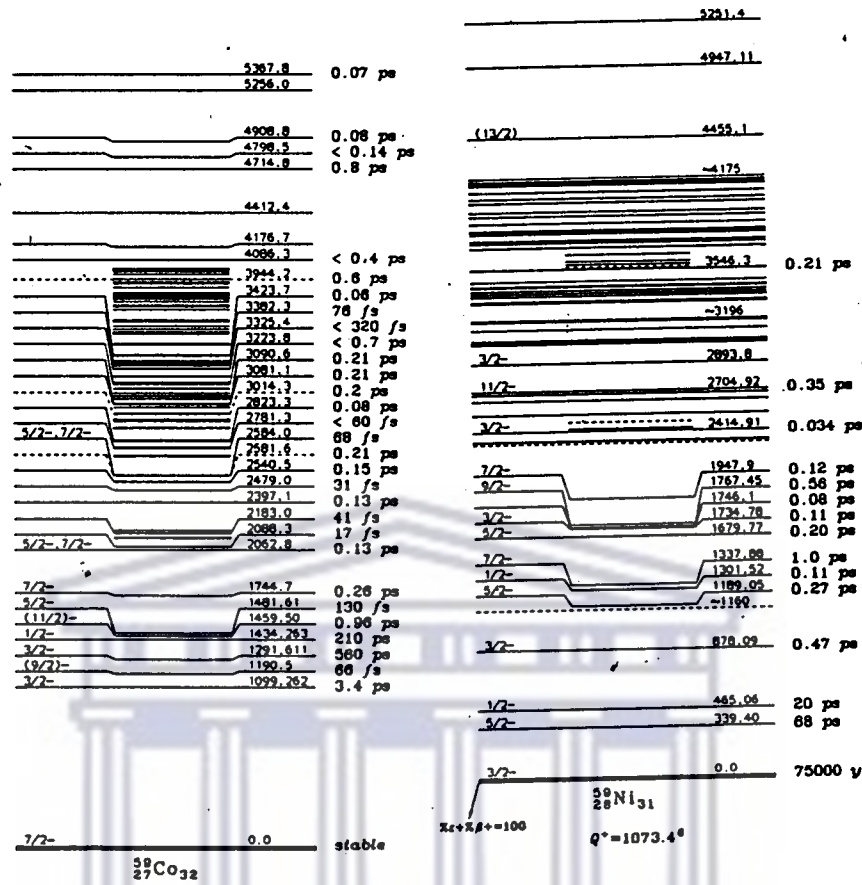
Figure 1.2: *Energy level diagrams for ^{59}Co and ^{59}Ni shown on an isobar diagram.*

The quenching of the Gamow-Teller strength has been interpreted as mixing of the GT nuclear excitations with the internal degrees of freedom (i.e., the Δ) [Wei83], but configuration mixing in these transitions is also important [Ari84]. As has been reported by [Rap83,Gaa84], it seems that up to about 20 MeV excitation energy, the quenching factor $Q_F = \sum B(GT)_{expt} / \sum B(GT)_{theor} = 0.65 \pm 0.05$, but due to the factors mentioned above this value fluctuates between ~ 0.4 and ~ 0.8.

The calculation of each β-decay transition strength is model dependent. However,

a model independent sum rule for the total strength states [Ikeda64] that

$$\sum B(GT)^- - \sum B(GT)^+ = 3(N - Z) \qquad (1.1)$$

$$\sum B(F)^- - \sum B(F)^+ = N - Z \qquad (1.2)$$

where Z and N are the proton and neutron numbers, and $B(F)$ and $B(GT)$ are the Fermi(F) and Gamow-Teller(GT) matrix elements respectively. In medium nuclei, such as iron, cobalt, etc., and heavy nuclei, such as zirconium, etc., the strengths of the Gamow-Teller matrix elements, $B(GT)^+$, are thought to be small due to Pauli blocking. This forms the subject of a related research project[a]. The Fermi strength is believed to be concentrated in a single narrow state: the Isobaric Analogue state (IAS) [And62]. It is thus of interest to measure both (p,n) and (n,p) cross sections on the same nucleus and to investigate the degree of quenching of the GT strength. These reactions types allow the study of isovector excitations without interference of isoscalar ones. In reaction such as (p,p') and (e,e'), isoscalar excitations can also be excited. Charge-exchange reactions on $N > Z$ nuclei with isospin T_o can excite states with isospin T_o and $T_o \pm 1$. From figure 1.1 it can be seen that, in the (n,p) reactions, only the $T_o + 1$ states can be excited. It can also be seen from the isospin Clebsch-Gordon[b] coefficients involved that the (p,p') reaction favours the population of T_o states; and (p,n) reactions that of $T_o - 1$ states. For large values of T_o, (p,n) transitions to $T_o + 1$ are inhibited by a large isospin factor. For (n,p) reactions the isospin factor is unity.

---

[a]The collaborators are: K Bharuth-Ram, IJ Lazarus, D Naidoo (UDW); IJ van Heerden (UWC); DG Aschman, RW Fearick, D Steyn (UCT); WR McMurray(NAC)

[b]The square of a Clebsch-Gordon coefficient represents the probability of finding the product state.

In order to test the sum rule and to determine the degree of quenching, a large data set which can be treated in a consistent way is desirable. Such a data set was obtained at the National Accelerator Centre (NAC), using the beam swinger and a bank of six plastic scintillator detectors. A ^{59}Co target, 44 mg/cm^2 thick, was bombarded at $\theta_{LAB} = 0°$ at four different incident proton energies, i.e 90 MeV, 120 MeV, 160 MeV and 200 MeV. At 120 MeV, 160 MeV and 200 MeV the experiment was also performed at $\theta_{LAB} = 2°$ and 4°.

Energy level diagrams for ^{59}Co and ^{59}Ni are shown in figure 1.2. As described in chapter 2, on the GT and F selection rules, the $\frac{3}{2}^-$ groundstate level of ^{59}Ni can not be excited by a GT or a F transition. However, the transition from the $\frac{7}{2}^-$ groundstate of ^{59}Co to the $\frac{5}{2}^-$ state at 0.34 MeV in ^{59}Ni is predominantly a $\Delta L=0$, $\Delta J=1$ and $\Delta S=1$ transition caused by the GT operators. In chapter 4 Shell-Model calculations of the Gamow-Teller strengths, $\sum B(GT)^-$, for this nucleus, are compared with the experimentally observed strengths.

Chapter 2

THEORETICAL BACKGROUND

The (p,n) reaction complements the $\beta-$ decay process. In this chapter I will discuss the relevant theory behind this process and give an overview of the interaction between the incoming nucleon and the target nucleons. I will discuss the advantages of using the (p,n) reaction as a Gamow-Teller probe and also look at the differential cross section formula given by the distorted-wave impulse approximation (DWIA).

2.1 Nuclear Beta Decay

$\beta-$ decay is the nuclear process in which a nucleus made up of Z protons and N neutrons decays to a nucleus of the same nucleon number A but with $(Z\pm1, N\mp1)$. A β^- decay,

$$n \rightarrow p + \bar{\nu} + e^-$$

(2.1)

Fermi(F)	Gamow-Teller(GT)
$\Delta S = 0$	$\Delta S = 0, \pm 1$ (but no $0 \rightarrow 0$)
$\Delta T = 0$	$\Delta T = 0, \pm 1$
$\Pi_i = \Pi_f$	$\Pi_i = \Pi_f$

Table 2.1: *Fermi and Gamow-Teller transitions selection rules*

may be regarded as the transformation of one of the neutrons in the nucleus to a proton and a β^+ decay,

$$p \rightarrow n + \nu + e^+ \tag{2.2}$$

as the transformation of a proton to a neutron. Since the leptons carry off very little momentum, the transition favours $L = 0$ (where L is the total angular momentum of the two lepton system with respect to the nucleus). Transitions of $L > 0$ are generally small and are said to be forbidden.

For the allowed decays, listed in Table 2.1, the nuclear part of the $\beta^{\pm}-$decay transition operator, $O(\beta)$, has the form,

$$O(\beta) = G_V \sum_{j=1}^{A} \tau_{\mp}(j) + G_A \sum_{j=1}^{A} \sigma(j)\tau_{\mp}(j). \tag{2.3}$$

The summation is over A nucleons constituting a particular nucleus. G_A is the axial vector coupling constant and G_V the vector coupling constant. The Gamow-Teller term involves both the spin operator, $\sigma(j)$, and isospin raising and lowering operator, $\tau(j)_{\mp}$. The Fermi (F) term involves only the isospin raising and lowering operator. Under the assumption that isospin is an exact quantum number,

	Target(^{59}Co)	Residual(^{59}Ni)	
		ground state	1st excited state
Spin(S)	$\frac{7}{2}$	$\frac{3}{2}$	$\frac{5}{2}$
Isospin(T)	$\frac{5}{2}$	$\frac{3}{2}$	$\frac{3}{2}$
Parity(π)	$-$	$-$	$-$

Table 2.2: *Properties of target and residual nucleus*

the Fermi matrix element, $G_V \sum_{j=1}^{A} \tau_{\mp}(j)$, can be evaluated without having to know explicitly what wave functions are involved [Wong90]. It was found that Fermi decay goes primarily between isobaric analogue states (IAS) where the only difference between the initial and final states is the replacement of a proton by a neutron or vice versa.

For the Gamow-Teller (GT) operator, $\sum_j \sigma(j)\tau_{\mp}(j)$, the summation over nucleons cannot be carried out explicitly, since both spin and isospin are acted upon at the same time. Unlike Fermi decays, matrix elements for the Gamow-Teller cannot be evaluated unless both the initial and final wave functions are given. The initial and final states are, therefore, related. The spins, isospins and parities of the target nucleus ground state and of the ground and first excited states of the product nucleus in the ^{59}Co(p,n)^{59}Ni reactions are listed in table 2.2. It is evident that the ground state of ^{59}Ni cannot be reached by the Gamow-Teller operator. The first excited state is, however, a possible Gamow-Teller transition.

Beta decay transition strengths can be deduced reliably [Wilk82,Bopp86] from beta decay lifetimes according to

$$B(F) + (1.260 \pm 0.008)^2 B(GT) = \frac{6166 \pm 2}{ft},\qquad(2.4)$$

where f is a calculable function that accounts for the phase space, t the measured half-life, B(F) and B(GT) the Fermi and Gamow-Teller matrix elements which are given by

$$B(F)^{\pm} = \frac{1}{2J_i + 1}|\langle f\|\sum_k \tau_k^{\pm}\|i\rangle|^2 \qquad(2.5)$$

$$B(GT)^{\pm} = \frac{1}{2J_i + 1}|\langle f\|\sum_k \sigma_k \tau_k^{\pm}\|i\rangle|^2. \qquad(2.6)$$

The reduced matrix elements are defined by Bohr and Mottelson [Bohr69] and $\tau_k^{\pm}$ is the kth raising or lowering operator.

2.2 Effective Nucleon-Nucleon interaction

In order to calculate and interpret nucleon-nucleus scattering in the intermediate energy range one has to have a knowledge of the coupling between the projectile and target nucleons [Love81,Love85]. The main distinction between nucleons (i.e protons and neutrons) is found in their electromagnetic properties: namely, charge and magnetic dipole moment. However, in nuclear forces, like in all strong interactions, such differences do not appear; i.e., in the absence of an electromagnetic interaction, a proton cannot be distinguished from a neutron. To calculate and understand nucleon-nucleus scattering, is, therefore, indeed a complex problem and we must be content with a phenomenological approach, namely that of obtaining the nucleon-nucleon, $\mathcal{NN}$, coupling from measurements of $\mathcal{NN}$ scattering observables.

It is widely believed that at intermediate energies the impulse approximation (IA) should provide a reasonable starting point. In the IA the effective interaction between the incident nucleon and each of the target nucleons is taken to be the t matrix of the free $\mathcal{N}\mathcal{N}$ interaction. For certain types of transitions, corrections to the $\mathcal{N}\mathcal{N}$ t matrix are known to be important. The two most important of these have been identified as

1. medium modifications due to Pauli blocking and short - range correlations, and

2. the use of a relativistic (Dirac) framework.

It is evident that, as more complete $\mathcal{N}\mathcal{N}$ information becomes available, the present interaction will have to be updated.

The effective interaction between the projectile (p) and the ith nucleon can be represented by a sum of three terms, the central (C) term, spin - orbit (LS) term, and the tensor (T) term:

$$V_{ip} = V^C(r_{ip}) + V^{LS}(r_{ip})\vec{L} \cdot \vec{S} + V^T(r_{ip})S_{ip}(\hat{r}_{ip}) \qquad (2.7)$$

where V^C, V^{LS}, and V^T depend on the isospin as well as the energy of the incident nucleon. The knock-on exchange terms are included either explicitly or implicitly via a short-range approximation [Petr80].

Some of the most important properties of the effective interaction can be understood by considering the modulus of the $\mathcal{N}\mathcal{N}$ t-matrix interaction as a function of momentum transfer (q), projectile kinetic energy (T_p) and spin and isospin transfers S and T. The energy dependence of the central parts of the $\mathcal{N}\mathcal{N}$ interaction at zero momentum transfer ($q = 0$) for $100 \leq T_p(MeV) \leq 800$ is illustrated in
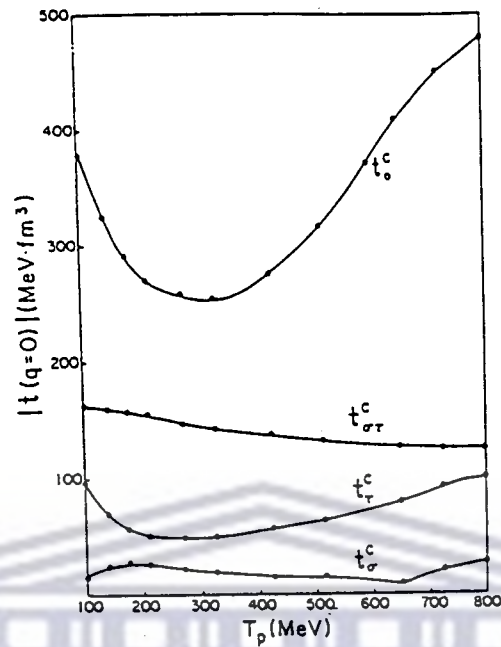
Figure 2.1: *Energy dependence of the magnitudes of the central (direct and exchange) parts of the $\mathcal{N}\mathcal{N}$ t matrix.*

Figure 2.1. Characteristic of this plot is the dominance of the scalar-isoscalar part t_o^C of $t_{\mathcal{N}\mathcal{N}}$ and the pronounced energy dependence of the t_τ^C (non-spin-flip) component [Love81]. By contrast, the energy dependence of the $t_{\sigma\tau}^C$ (spin-flip) component is seen to be very weak between 100 and 800 MeV. The isovector amplitudes t_τ^C and $t_{\sigma\tau}^C$ drive the (p,n) reaction, since charge-exchange reactions filter out the otherwise dominant t_o term. The dominance of $t_{\sigma\tau}^C$ between 100 and 500 MeV incident energies, due to the sharp decrease in t_τ^C above $\sim$50 MeV, has been widely exploited in the interpretation of isovector spin modes in charge-exchange reactions [Good80], since one may selectively excite different types of states.

A quantity which has been particularly useful in the identification and interpretation of isovector excitations, is the ratio $|t_{\sigma\tau}/t_\tau|^2$ at $q = 0$. The energy dependence
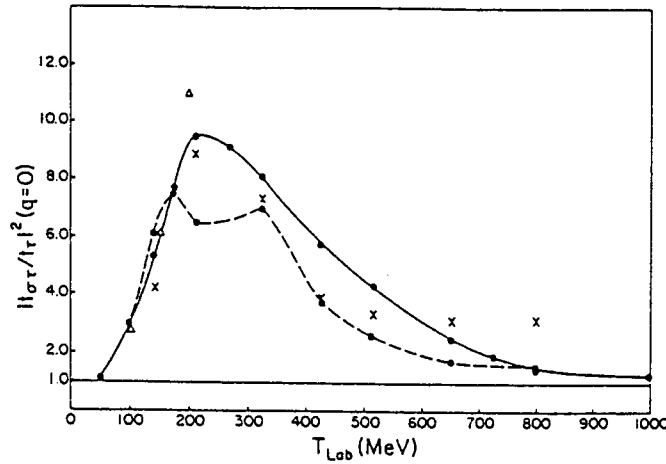
Figure 2.2: *Energy dependence of the ratio* $|t_{\sigma\tau}(q=0)/t_\tau(q=0)|^2$. *The lines represent impulse approximation calculations as described in the text.* $\triangle$ *and* x *are experimental data [Tadd81].*

of this quantity is shown in Figure 2.2 for the $\mathcal{NN}$ amplitudes based on the 1979 phase parameters of Arndt *et al.* [Arnd83] and of Bugg *et al.* [Bugg80], the dashed curve, as well as for the 1984 SP84 $\mathcal{NN}$ amplitudes, the solid curve. The ratios based on the SP84 amplitudes agree well with experimental values [Tadd81] extracted from the (p,n) reactions below $\sim$200 MeV [Love87]. This ratio determines to a large extent which type of mode ($\triangle S = 1$ or $\triangle S = 0$) should dominate the spectrum at a given beam energy.

2.3 The (p,n) reaction as a Gamow-Teller probe

After simple corrections for distortion effects [Good80], 0° (p,n) reactions are found to be proportional to the squares of the corresponding Fermi and Gamow-Teller matrix elements extracted from β-decay measurements. This correspondence derives from the similarity of the operators involved in each type of reaction. The isovector terms in the effective $\mathcal{NN}$ interaction that mediate low momentum
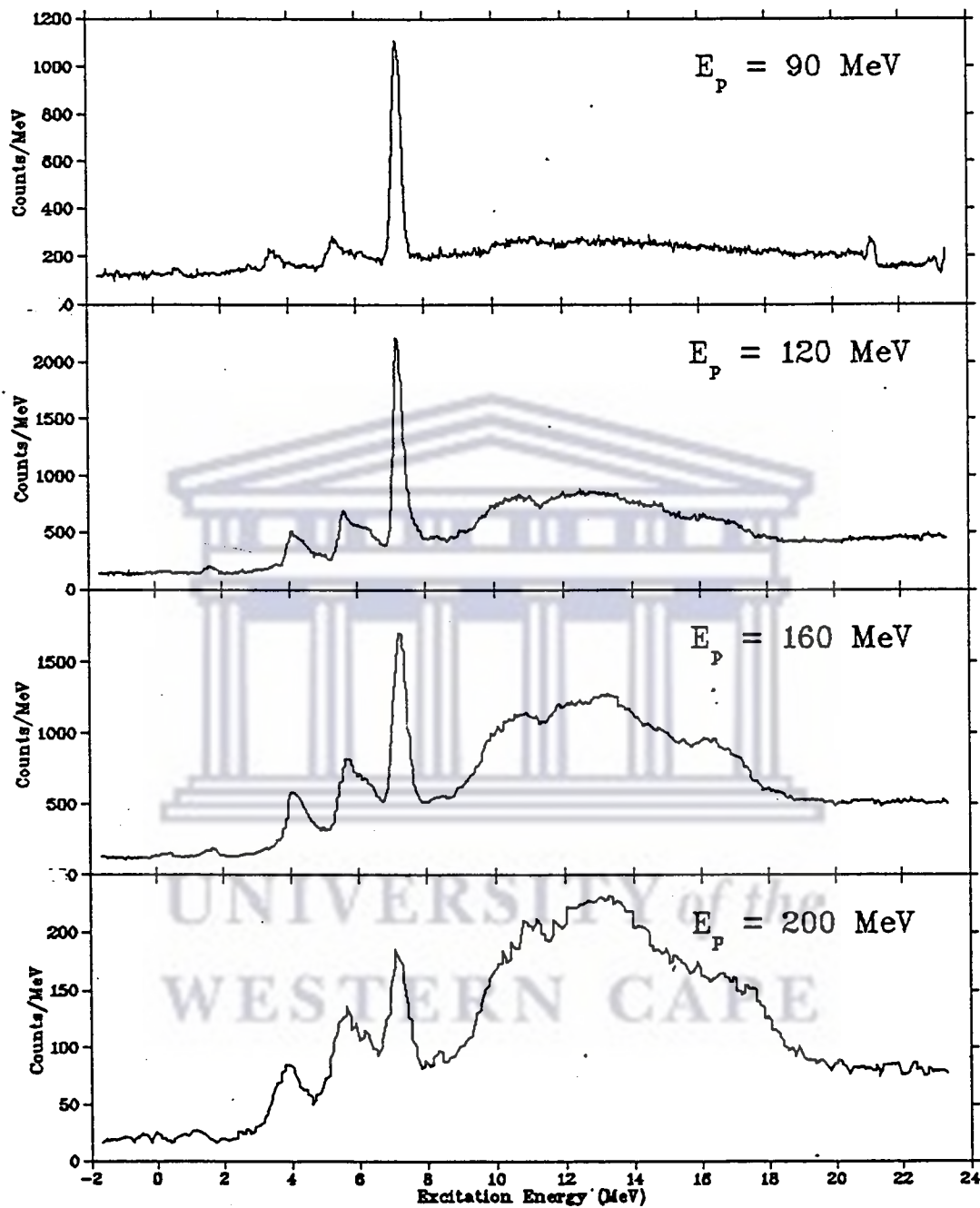
Figure 2.3: *The (p,n) reaction on ^{59}Co as a function of bombarding energy showing the relative dominance of Fermi and GT transitions.*

transfer spin-flip ($\triangle$S=1) transitions,

$$\sum_i V_{\sigma\tau}(r_{ip})\sigma_i \cdot \sigma_p \tau_i \cdot \tau_p,$$

and non-spin-flip ($\triangle$S=0) transitions,

$$\sum_i V_\tau(r_{ip})\tau_i \cdot \tau_p,$$

are similar to the corresponding operators

$$G_A \sum_i \sigma_i \tau_i^\pm \text{ and } G_V \sum_i \tau_i^\pm$$

for Gamow-Teller and Fermi β-decay, respectively [Tadd87].

At energies larger than about 50 MeV the isovector spin-flip component of the effective interaction dominates over the non-spin-flip component. At intermediate energies and at $\theta = 0°$ (momentum transfer $q = 0$), where tensor, spin-orbit, and other $L > 0$ effects are generally small, this leads to the selective spin-flip excitations [Love81] of states that are connected to the target ground state by transitions analogous to GT β-decay. Since the (p,n) reaction is not subjected to the energetic limitations of β-decay, it therefore can be used to probe the entire GT strength.

2.4   Isovector excitations at small momentum transfers

In the distorted-wave approximation the differential cross section is given by [Satch64]

$$\frac{d\sigma}{d\Omega} = \left(\frac{\mu}{2\pi\hbar^2}\right)^2 \frac{k_f}{k_i} \frac{1}{(2J_i+1)(2s_p+1)} \Sigma | \int \chi_f^{(-)*}(\bar{r}_p) < f|\sum_j v_{jp}(1-P_{jp})|i > \chi_i^{(+)}(\bar{r}_p)d^3r_p|^2,$$

$$(2.8)$$

where μ denotes the reduced energy devided by c^2 and k the wave number, in the centre of mass. J_i is the total angular momentum and s_p the intrinsic spin of the incident projectile. The χ's are the distorted waves, $< f| \sum_j v_{jp}(1 - P_{jp})|i >$ the target matrix element, v_{jp} the effective nucleon-nucleon interaction, P_{jp} the permutation operator accounting for knock-out exchange, and the sum outside the absolute value brackets is over the initial- and final-spin projections of the projectile and target.

The time-of-flight technique used for (p,n) studies permits measurements of cross sections at $0°$ where the (p,n) preferentially populates transitions with appreciable Fermi and Gamow-Teller matrix elements. The (p,n) reaction selects the isovector $(\triangle T = 1)$ parts of the effective nucleon-nucleon interaction and for $0°$ scattering, the low momentum transfer components provide the dominant contributions to the transition amplitude. With this simplification [Good80] the $0°$ cross sections for (p,n) transitions with Fermi and/or Gamow-Teller strength can be described by [Petr69]

$$\frac{d\sigma}{d\Omega}(0°) = \left(\frac{\mu}{\pi\hbar^2}\right)^2 \frac{k_f}{k_i} \left[N_\tau |J_\tau|^2 B(F) + N_{\sigma\tau} |J_{\sigma\tau}|^2 B(GT) \right], \qquad (2.9)$$

where N_τ and $N_{\sigma\tau}$ are the distortion factors which account for the incident flux loss due to the scattering process, and J_τ and $J_{\sigma\tau}$ represent the volume integrals $(q = 0$ component) of the central isovector non-spin-flip and spin-flip parts of the effective nucleon-nucleon interaction respectively.

The equation 2.9 is for a mixed (F and GT) transition as occurs in odd nuclei. For a pure transition (of type α),

$$\sigma(\alpha) = \frac{d\sigma}{d\Omega}(0°, \alpha) = K_\alpha N_\alpha B(\alpha)|J_\alpha|^2, \qquad (2.10)$$

with

$$K_\alpha = \left(\frac{\mu}{\pi\hbar}\right)^2 \frac{k_f}{k_i}.$$ (2.11)

For two such transitions at 0°,

$$\frac{B(GT)}{B(F)}\left|\frac{J_{\sigma\tau}}{J_\tau}\right|^2 = \frac{\sigma_{GT}}{\sigma_F}\frac{K_F}{K_{GT}}\frac{N_F}{N_{GT}}.$$ (2.12)

The ratio $|J_{\sigma\tau}/J_\tau|$ can to a large [Tadd87] extent determine the GT and F interaction strengths. The reason for this is that the ratio B(GT)/B(F) is known from β-decay, the ratio of the corresponding 0° (p,n) cross sections can be measured, the K_{GT} and K_F terms are easily calculable kinematic factors, and one can make a reasonable estimate of the ratio of the distortion factors N_F/N_{GT}.

From equation 2.10 it can be seen that the proportionality factor $\hat{\sigma}(\alpha)$, with $\alpha = GT$ or F, can be expressed as

$$\hat{\sigma}(\alpha) \equiv \frac{\sigma(\alpha)}{B(\alpha)} = K_\alpha N_\alpha |J_\alpha|^2.$$ (2.13)

This proportionality factor is also called the unit cross section and is known to be dependent on the bombarding energy as well as on the target nucleus. From reference [Tadd87] it is apparent that the bombarding energy dependence comes from the K_α and the A (target) dependence from N_α.

Taddeucci *et al.* [Tadd81,Tadd87] have found that the ratio of $\hat{\sigma}_{GT}$ to $\hat{\sigma}_F$

$$R_{E_p}^2 \equiv \frac{\hat{\sigma}_{GT}}{\hat{\sigma}_F} = \frac{\sigma_{GT}(0°)}{\sigma_F(0°)}\frac{B(F)}{B(GT)}\frac{K_F}{K_{GT}}$$ (2.14)

is simply related to the proton bombarding energy

$$R_{E_p} = \frac{E_p}{55.0 \pm 0.4 MeV}.$$ (2.15)

This is, however, only true (see figure 2.4) for even-mass nuclei. Further measurement has shown that for odd-mass nuclei [Hua91] the following formula,

$$R_{E_p} = \frac{E_p}{45.0 \pm 0.6 MeV},$$ (2.16)
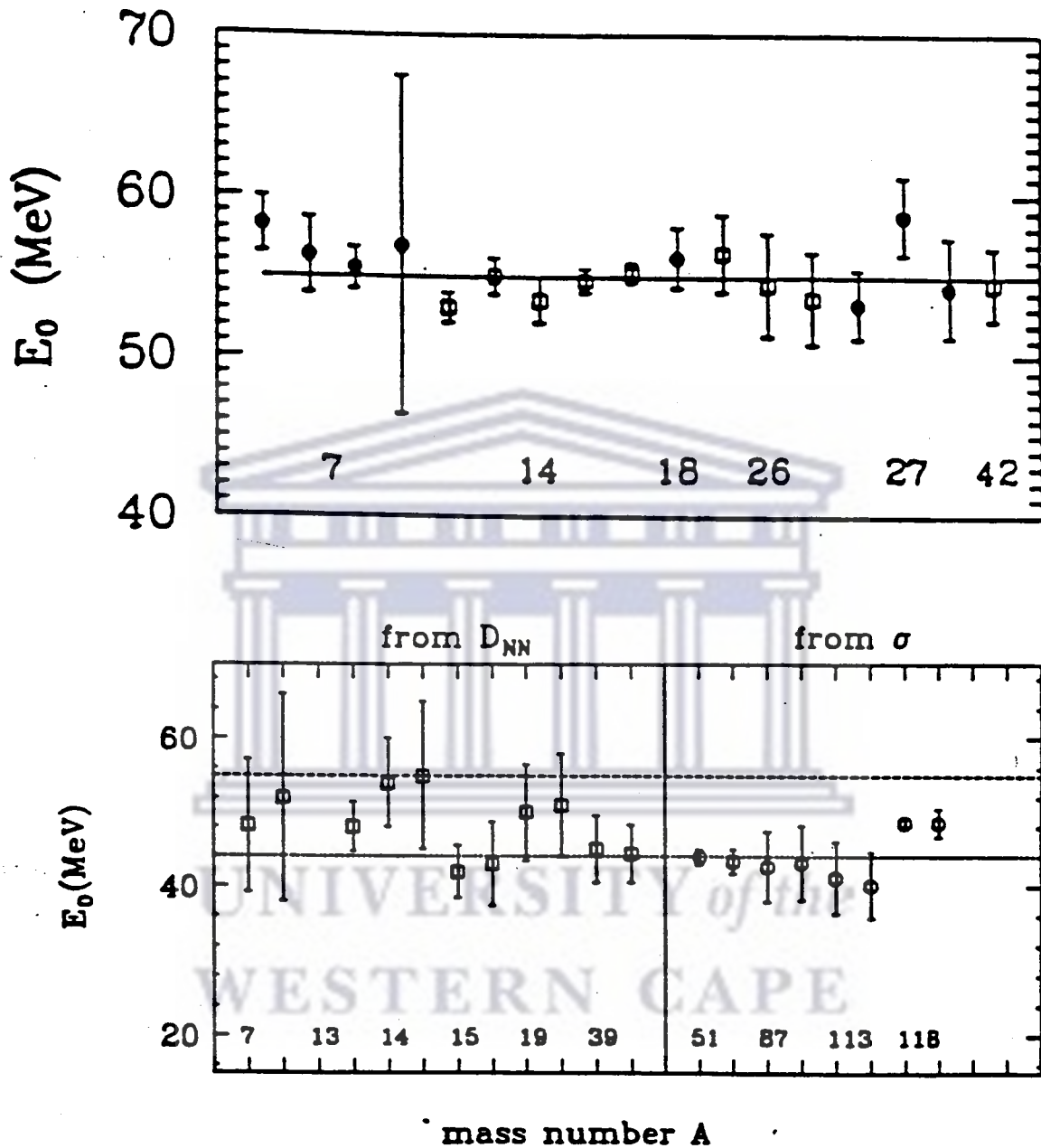
Figure 2.4: *(a) Slope parameter $E_o = E_p/R_{E_p}$ determined from cross section measurement for even-mass nuclei. (b) Same E_o determined from cross section and polarization transfer, $D_{NN}(\theta°)$, measurements for odd-mass nuclei.*
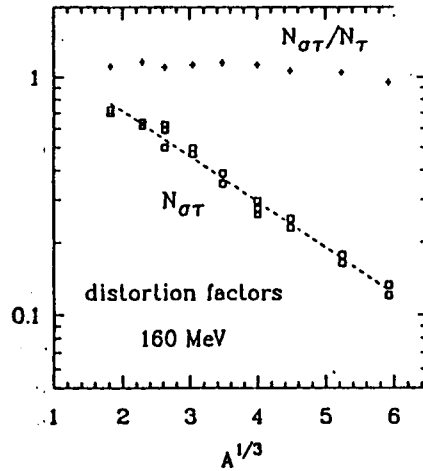
Figure   2.5:   *Distortion   factors   calculated   according   to*
$N^D = \sigma(DW; 0°)/\sigma(PW; 0°)$

is applicable. From equation 2.10 R_{E_p} may be interpreted as the ratio

$$R_{E_p} \approx \frac{|J_{\sigma\tau}|}{|J_\tau|} \left(\frac{N_{\sigma\tau}}{N_\tau}\right)^{\frac{1}{2}}. \tag{2.17}$$

At intermediate energies, the ratio of the distortion factors is close to unity (see figure 2.5). The value $R^2_{E_p}$, therefore, measures the effectiveness of the (p,n) reaction in producing spin-flip (GT) transitions relative to analog (F) transitions. If the momentum transfer (q) is limited to zero, and the two states are sufficiently close so that the energy loss (ω) between the IAS and the reference GT state is small, then

$$K_F/K_{GT} \rightarrow 1. \qquad \text{as } (q,\omega) \rightarrow 0$$

Therefore, equation 2.14 is reduced to a simpler definition

$$R^2_{E_p} = \frac{\sigma_{GT}(q = 0)}{\sigma_F(q = 0)} \frac{B(F)}{B(GT)} \tag{2.18}$$

However, equation 2.18 must be modified for odd-A targets, since mixed transitions are possible. The cross sections for a mixed GT + F isobaric analogue

transition and a nearby pure GT transition may be used if

$$R_{E_p}^2 = \frac{\sigma_{GT}(q=0)}{\sigma_{IAS}(q=0)} \frac{N-Z}{B_1(GT)} \left[1 - \frac{\sigma_{GT}(q=0)}{\sigma_{IAS}(q=0)} \frac{B_0(GT)}{B_1(GT)} \right]^{-1} , \qquad (2.19)$$

where the subscripts '0' and '1' refer to the IAS and the pure GT transition, respectively.

Chapter 3

EXPERIMENTAL DESCRIPTION

3.1 Introduction

This experiment requires the detection of neutrons. One of the main problems in detecting neutrons is that they are electrically neutral. It is, therefore, impossible to implement the standard methods used to detect charged particles, such as electro-magnetic and direct ionization spectrometers. Another problem encountered in detecting neutrons with high resolution and reasonable efficiencies is the high levels of background radiation. In spite of these problems, several methods of neutron spectroscopy have been developed including:

1. the measurement of proton recoil energies;

2. the measurement of the energy released in a known nuclear reaction;

3. diffraction in crystals at very low energies; and

4. the time-of-flight measurement.

The most successful method of measuring neutron energy is the time-of-flight technique. However, the disadvantage of this particular method is that it needs a long flight path to achieve the necessary energy resolution and this leads to a very small solid angle and, therefore, low neutron flux.

The time-of-flight technique allows the neutron to interact with matter and produce charged particles. The latter can then be detected by standard methods. For example, the neutron interacts either with hydrogen or carbon in a scintillator through the following nuclear reactions, neutron-proton scattering, $^{12}C(n,x)$ reactions or elastic scattering.

By making use of the neutron-time-of-flight (NTOF) facilities at the National Acceleration Centre (NAC) in Faure (RSA), we were able to successfully carry out the experimental work on the $^{59}Co(p,n)^{59}Ni$ reaction.
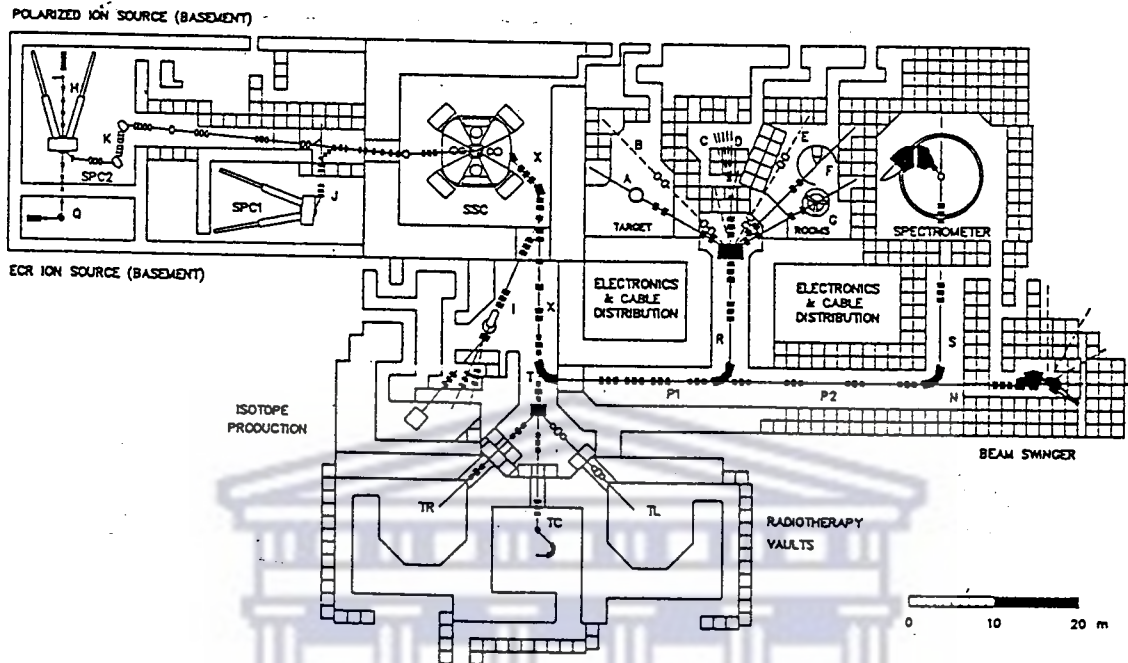
. Figure 3.1: *Cyclotron facility at the National Acceleration Centre.*

3.2 The Facility

The experiment was carried out at the 200 MeV cyclotron facility at the National Acceleration Centre (NAC) in Faure [Bot86a]. A layout of this facility is shown in figure 3.1. A detector station located outside the experimental hall was used. This station is located along the $0°$ line with respect to the incident proton beam and was placed at a distance of $\sim$174m from the target. A typical time resolution of 1.0-1.2ns (fwhm) was obtained which, for 200 MeV protons, corresponds to an energy resolution of $\sim$430 keV. Calculations have shown that with a reduced flight path reasonable energy resolution can be still be obtained. The calculated energy resolutions at different beam energies are plotted in figure
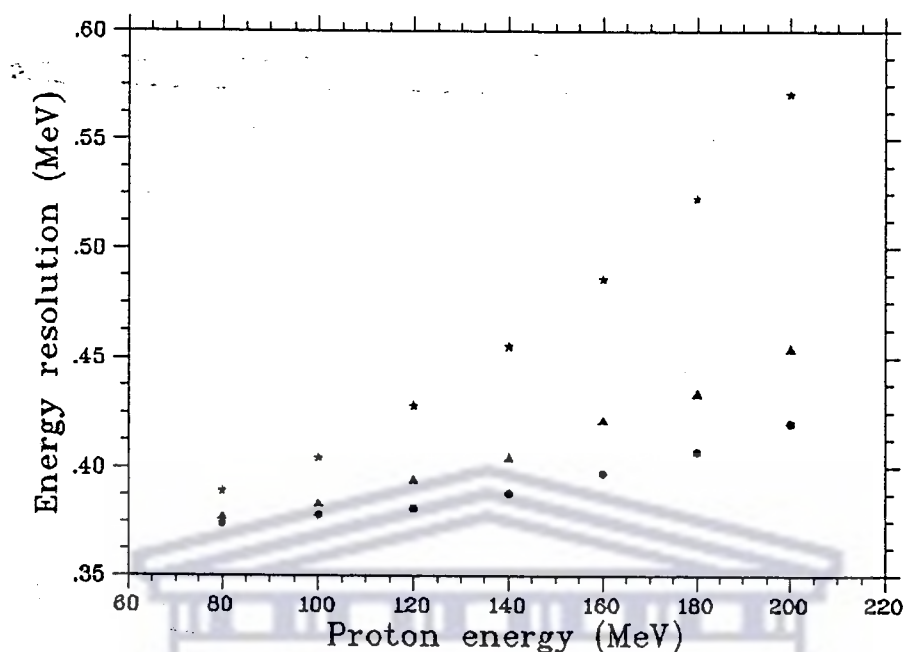
Figure 3.2: *Energy dependence of the overall energy resolution at flight paths of 174m (•), 130m (△) and 80m (⋆)*

3.2. These calculations have been done at three different flight paths, i.e. 80, 130, and 174m. At a distance of ~80m from the target and incident energy of about 120 MeV an energy resolution of ~0.377 MeV can be achieved. The energy resolution increases to ~0.571 MeV at an incident energy of about 200 MeV. These calculations were carried out using the measured intrinsic time resolution of the detectors (~350ps, fwhm), the measured beam time spread (~350ps), and using an overall energy resolution of 370 keV to calculate the overall time resolution. A reduced flight path has the advantage that the wrap around background will be reduced (giving "clearer" spectra), and that the solid angle will be increased (giving a higher count rate).

A Solid Pole injector cyclotron (SPC1) with an internal ion source, capable
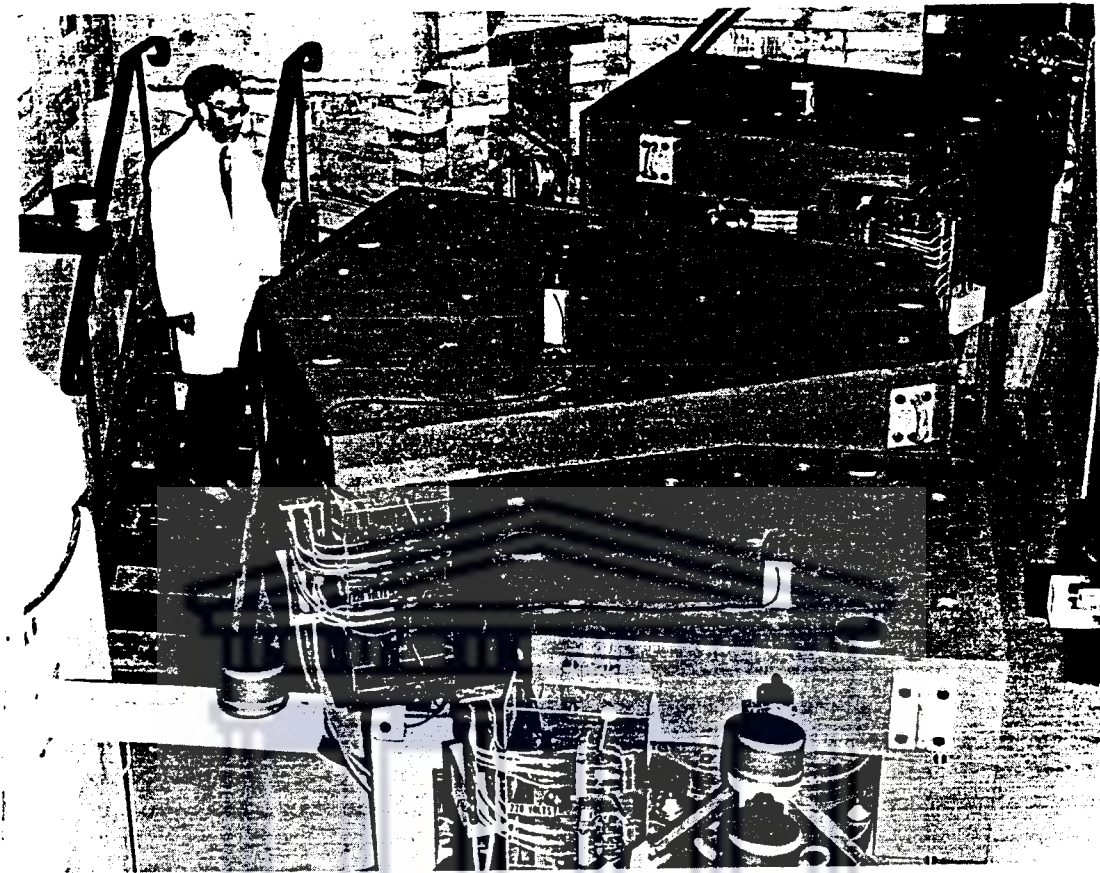
Figure 3.3: *The three dipole magnets forming the beam swinger: B1N (front), B2N (centre) and the dump magnet B3N (top).*

of producing unpolarized light ions, accelerates protons to a maximum energy of 8 MeV for injection into the first orbit of the Separated - Sector cyclotron (SSC) in which the protons can be accelerated to a maximum energy of 200 MeV. A second injector cyclotron which is still under construction [Bot86b] will be able to produce polarized beams and heavy ion beams. Charged particles are extracted from the SSC and transported via high energy beam lines through a 90° analyzing magnet before being directed into the beam swinger. The target ladder and the beam swinger are placed in a vault at the end of beam line N. During the experiments an average machine vacuum of 5.0×10^{-5}Pa is maintained [NAC90].
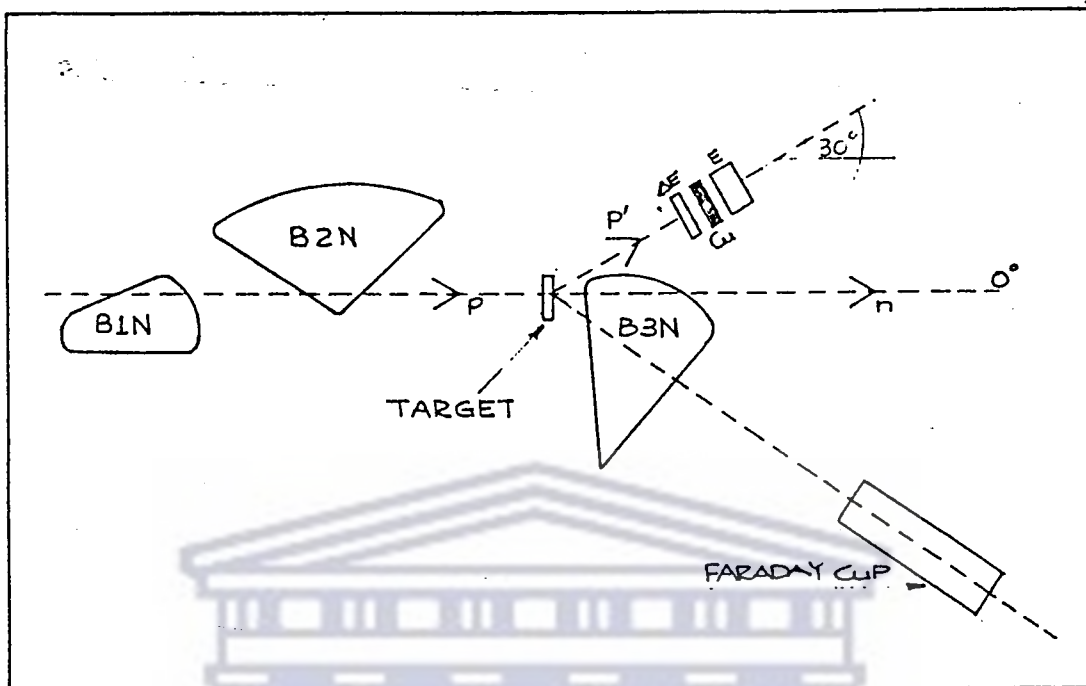
Figure 3.4: *Schematical diagram showing the three dipole magnets as well as the location of the target, the proton telescope and the Faraday cup.*

Since the detector remains fixed in space, the beam swinger must be used to change the angle at which the beam hits the target to obtain angular distributions. The swinger is equipped with a 6-position target holder, which uses a stepping motor and shaft-encoder to position the targets. The beam swinger consists [NAC90] essentially of three dipole magnets: two bending magnets and one beam-dump magnet. The first circular-pole magnet (B1N) deflects the beam away from the beam line. The second magnet (B2N) is a specially-contoured wedge magnet which bends the beam back to the beam line and focuses it onto the target. The angle of incidence is continuously variable over a range of about 30° by varying the amount of bend. The third magnet (B3N) swings those charged particles that have not interacted with the target away from the 0° flight path,

and focuses these particles onto the Faraday cup [a] situated in the beam dump. The Faraday cup is connected to a current integration unit (BIC 1000c) via a Faraday cup relay interface (EDA 14-2) and a current integrator interface (EDA 14-3).

Neutrons destined to reach the detectors had to pass through a narrow collimator (with dimensions ± 6.0m x 0.1m x 0.1m) in the shield wall of the swinger area.

3.3   Pulse Selection

In order to obtain a "clean" spectrum one has to reduce the wrap around background. This background arises from slow neutrons of earlier beam bursts. The magnitude of this problem depends on the pulse separation, the flight path and the energy threshold of the detector. However, if the energy-thresholds of the detectors are raised to reduce wrap around, the efficiency of the detector is reduced dramatically. Increasing the time between two consecutive pulses is a more effective way to counteract this problem.

Two 1.50m long water-cooled deflection plates are positioned [NAC87] over the beam path at its point of entry in the south valley chamber of the SSC. The positioning of the deflection plates is pneumatically controlled in order to position the plates. For pulse selection the deflection plates are positioned 40 mm apart. The pulse selector has been used over a wide energy range up to 200 MeV and with selection factors from 1:5 to 1:7. With a pulse selection of 1:7 at 200 MeV the selector frequency is 3.714 MHz. However, because of the long flight path and

---

[a]see figure 3.4

high proton energies used, a separation of ~270ns between pulses is insufficient to entirely eliminate wrap around. This is one of the main motivations to reduce the flight path.

3.4   Proton Telescope

In order to determine the time-of-flight of the neutrons, we need to know when the neutron started its flight. These "start" pulses for the time-to-digital converters are derived from the cyclotron pulse selected radio frequency (PSRF). Although the PSRF signal is generated when a proton bunch is extracted from the SSC and not when a (p,n) reaction actually occurs, this presents no difficulty since the timing is relative. In conjunction with a signal produced by a proton telescope setup viewing the target, the PSRF signal can be used to measure the beam bunch width on the target. It is important to measure this beam time spread because it is one of the factors contributing to the overall timing uncertainty. With this setup one can check whether beam quality changes with time and also monitor the phase stability. If any significant phase shifts occurred during a run it is possible to correct for that off-line. By deviding the run into a number of sections and shifting the different sections into phase with one another it is possible to counteract the problem.

Fast protons elastically scattered from the target are detected in a fast plastic scintillator system consisting of ΔE and E [b] detectors, located along a 30° line with respect to the undeflected proton beam at a distance of about 1m from the target in the beamline N vault. Two detectors are used for this setup. The detectors consists of a NE102A scintillator (~1cm thick) coupled to a R329 two

---

[b]see figure 3.4 for spatial relation of the proton telescope to the target and the beam swinger

inch (2") Hamamatsu photomultiplier tube with a E931 base. At high beam energies (160 MeV and 200 MeV) a Cu block (2.5cm thick degrader) was placed between the ΔE detector and the E detector to degrade the elastically scattered protons sufficiently for them to stop in the E detector. This set up provides a means of measuring and monitoring the beam time spread. The beam time spread, however, is dependent on operational factors. Beam time spreads of about 350ps were measured.

3.5   Detector Station

Count rate (efficiency) and time resolution (energy) are of the major considerations when designing a detector system. A trade-off between these two factors is necessary since a reasonable time resolution generally requires a longer flight path, while, on the other hand, the event rate is reduced because the smaller solid angle subtended by the detectors at the target.

To compensate for the rate loss, the size of the detector should be increased. But increasing the size of the detector degrades the time resolution. The reason for this is that the intrinsic time resolution of the detectors depends on the light collection time. This is purely a geometrical effect as shown in figure 3.5. The arrival time of a light signal at the photomultiplier tube at each end depends on its actual flight path through the detector. Different flight paths introduce a time uncertainty, and this has a definite effect on the time resolution of the detector. To improve this, construction of another detector with parabolic shaped light guides whereby rays making a large angle Θ with the centre axis of the detector are prevented from reaching the photomultiplier tubes, is currently underway. Other factors [Bre87] influencing the intrinsic time resolution of the detectors,
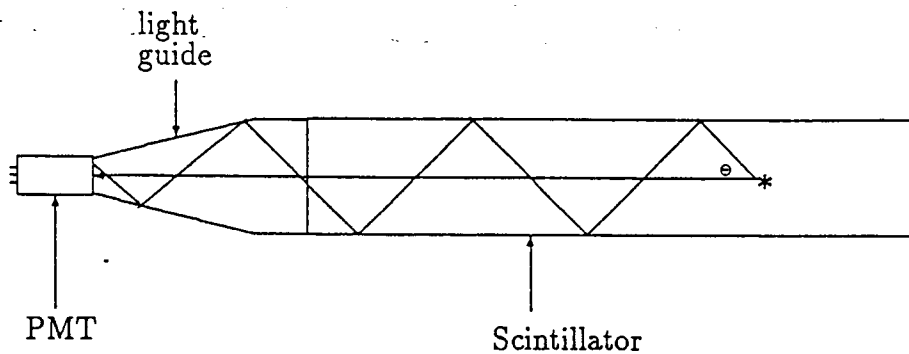
Figure 3.5: *Two different light rays from one point in the scintillator follow different paths with different arrival times.*

are:

1. the interaction time with the scintillator material (negligible);

2. scintillator rise- and decay time;

3. the attenuation length of the detector (most important parameter in dictating choice); and

4. the photomultiplier tube (PMT) characteristics.

3.5.1   The Detector

Six detectors are installed on top of each other in the detector hut. Each detector consists of a plastic scintillator (NE102A), with dimensions 60cm x 10cm x 10cm, viewed at either end with a 2" diameter PMT (Hamamatsu R329) mounted on a E931 base via a conically shaped lucite light guide (see figure 3.6). The PMT's are coupled to the light guides and the latter to the scintillator with silicone grease

silicone couplings
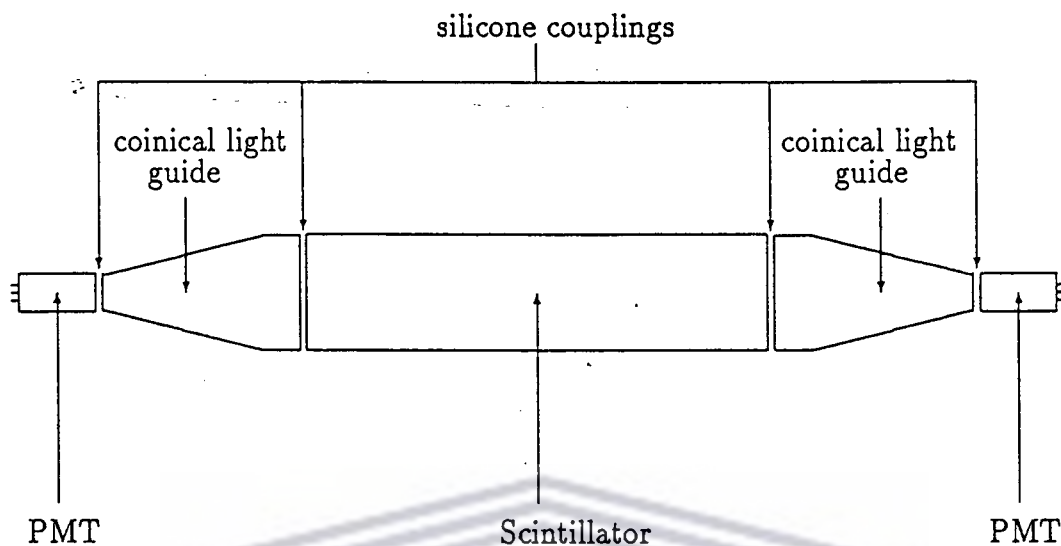
Figure 3.6: *Cross sectional view of the detector.*

(NE 836). When a particle hits the plastic scintillator, light is emitted, and transmitted along the detector before reaching the photocathodes via the light guides. The photocathodes convert part of the photon energy into electrons and the PMT's convert the light signal into an electrical signal. To ensure that the detector is light-tight, it is wrapped with a black sheet, placed in an aluminium casing, and wrapped again with black plastic.

3.5.2 Instrumental Calibrations

Unbalanced and unstable detector gains will produce unequal shapes of pulse height spectra. With the help of cosmic rays, gains are monitored and set off-line. A high energy muon entering the detector stack vertically, will fire all six detectors almost simultaneously. The energy deposited in each detector follows a minimum ionizing process which is roughly the same in all the detectors. Such cosmic rays, therefore, can serve as energy reference signals and are used for gain balancing as well as to calculate the intrinsic time resolution of the detectors.

The big advantage of cosmic rays is that the signal is always available and that they arrive with a reasonable event rate. The overall as well as the relative gains are balanced by changing the high voltages applied to the phototubes, to ensure equal pulse heights at the analog-to-digital converters (ADC's, LeCroy 2249A). An IBM compatible PC is used to set the high voltages.

3.6   Electronics

The main electronics are set up in the detector hut and all the timing signals are then carried via cables to the data room where the experiment is controlled.

3.6.1   Detector hut

A schematic diagram of the main electronics is shown in figure 3.7. Each PMT has two output signals. The one anode signal ($A_{1,1}$) is delayed, attenuated (EDA 29 passive switch attenuator) and then fed to an ADC to be used for pulse height analysis. The other anode pulse ($A_{2,1}$) is split into two signals by 6dB splitters for timing analysis. The diagram shows the cosmic-6 event trigger logic (left), and the neutron event trigger logic (right).

Cosmic-6 event

The timing signals that are derived from a Constant Fraction Discriminator (CFD, Ortec934), delayed and sent to the time-to-digital converters (TDC's, LeCroy 2228A) as a stop signal. For each detector, a required coincidence between left and right PMT CFD outputs is generated by an Octal mean timer (Lecroy 624) to indicate whether the detector has fired. The mean timer outputs of the top three detectors are fed into a 4-Fold-Logic (LeCroy 365AL) unit with coincidence level set to three. The other mean timer outputs are discriminated

Figure 3.7: *Main electronic set up (detector hut)*

and become inputs of the pattern register which indicates which detector has fired. The same procedure is invoked on the mean timer outputs of the bottom three detectors in order to generate another threefold coincidence. These two outputs are fed into another 4-Fold-Logic unit to determine whether it is a cosmic-6 event. Thus, a cosmic event occurs only when all six detectors are triggered simultaneously. One output of this module is fed to a pattern register and another one is used in conjunction with the neutron signal to generate an event trigger.

Neutron event

The other signals from the splitter are fed into a Quad linear gate (Phillips 744) and are then fed into a 6-channel discriminator (Phillips 711). By setting the threshold energies ($\sim$45 MeV) high, extraction of the high energy (neutron) events are possible, therefore eliminating all the low energy background events. If the threshold energy is too high, wrap around is reduced but the event count rate is then too low. Whenever the summed output pulse voltage from this module is bigger than 50 mV it indicates that an event above threshold has occurred in one of the detectors. The summed output of the 6-channel discriminator is then fed into a Quad discriminator to convert the analog input signal into a standardized output pulse.

"Wide" trigger

Both the neutron signal and the cosmic-6 signal are fed into a 4-Fold-Logic unit with coincidence level set to one. Therefore, for any event that has occurred (whether cosmic-6 or neutron) the times are stored onto magnetic tape. However, when analyzing the data the cosmic-6 events are extracted from the data base by making use of the fact that an event is cosmic-6 if all six detectors are

triggered simultaneously.

This signal is fed into a Quad discriminator where the discriminated output pulse is stretched. The width of the "wide" trigger is set to just less than the period of the PSRF, therefore, ensuring that there is not more then one start pulse for every stop pulse. For example, at 200 MeV proton energy, a pulse selection of 1:7 was used corresponding to a PSRF period of 269.3ns. The PSRF signal from the cyclotron is delayed to fall inside the stretched pulse and these signals are then fed into a 4-Fold-Logic unit set on a coincidence level 2. The output of this module, which was vetoed by the computer busy signal (supplied by the event trigger module) is fed to a discriminator. This discriminated output pulse is then used for the event trigger, the ADC gate, the TDC start signal and for the pattern register strobe.

3.6.2 ΔE-E beam

Since the overall time dispersion is the quadrature sum of the beam time spread, intrinsic time dispersion of the detectors and other factors, it is necessary to monitor and measure the beam time spread. This set up supplied the means to do that. Only fast protons elastically scattered from the target at an angle of 30° are detected.

Two Ortec 536's supplied the High Voltages (HV) to the bases of the NaI detectors. A block diagram of the ΔE-E electronics is shown in figure 3.8. The raw ΔE signal is fed into a splitter (6dB, 50 Ohm) and then through a Constant Fraction Discriminator (CFD, Ortec 583) which enabled us to set a window on the elastically scattered protons. This output signal is furthermore fed into a Quad discriminator (Lecroy 821), through a delay box and then into a 4-Fold-logic unit
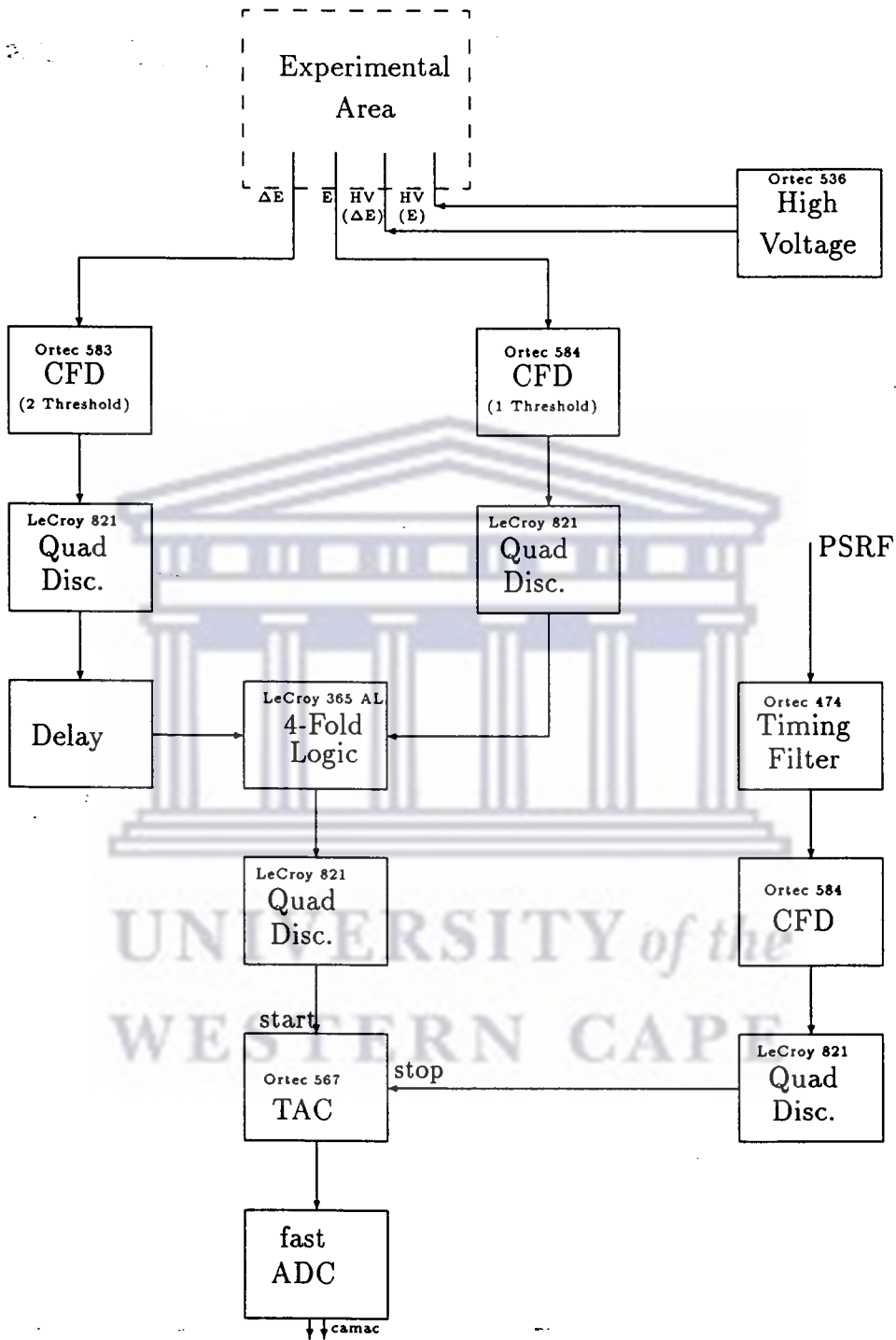
Figure 3.8: *Electronics: ΔE-E beam*

with a twofold coincidence level. The discriminated E signal is obtained by sending the raw E signal through another 6dB 50 Ohm splitter and then through a CFD (Ortec 584). The Ortec 584 has only one pulse height threshold setting and by setting the threshold sufficiently high, all the low energy, elastically scattered protons are extracted. This output signal is fed through a Quad discriminator to the 4-Fold-logic unit mentioned above. By delaying the ΔE signal sufficiently, we ensure that the two timing signals are in coincidence.

In order to optimize the ΔE-E signal generated by this set up, the raw E signal triggered with the discriminated E signal, is observed on a fast oscilloscope (300 MHz). By setting the pulse height threshold high, only fast elastically scattered protons are detected by the proton telescope. The raw ΔE signal, triggered with the discriminated E signal, is then observed. We then set the ΔE signal around the observed pulse height band by looking at the raw ΔE, triggered on the discriminated ΔE and changing the upper and lower pulse height settings of the CFD (Ortec 583).

The output pulse of the 4-Fold-logic unit is discriminated and used as the start gate of a Time-to-Amplitude converter (TAC, Ortec 567). A discriminated PSRF pulse is used as the stop signal to the TAC. Signals from the latter module are fed to the inputs of fast Analog-to-digital converters (ADC's). After digitation, the signals are sent to the VAX-11/730 computer via Camac and a microprogrammable branch driver (MBD-11).

3.6.3   Dead time

The largest contribution to dead time comes from the ADC conversion time plus the time required for the computer to read the event data from the Camac sys-
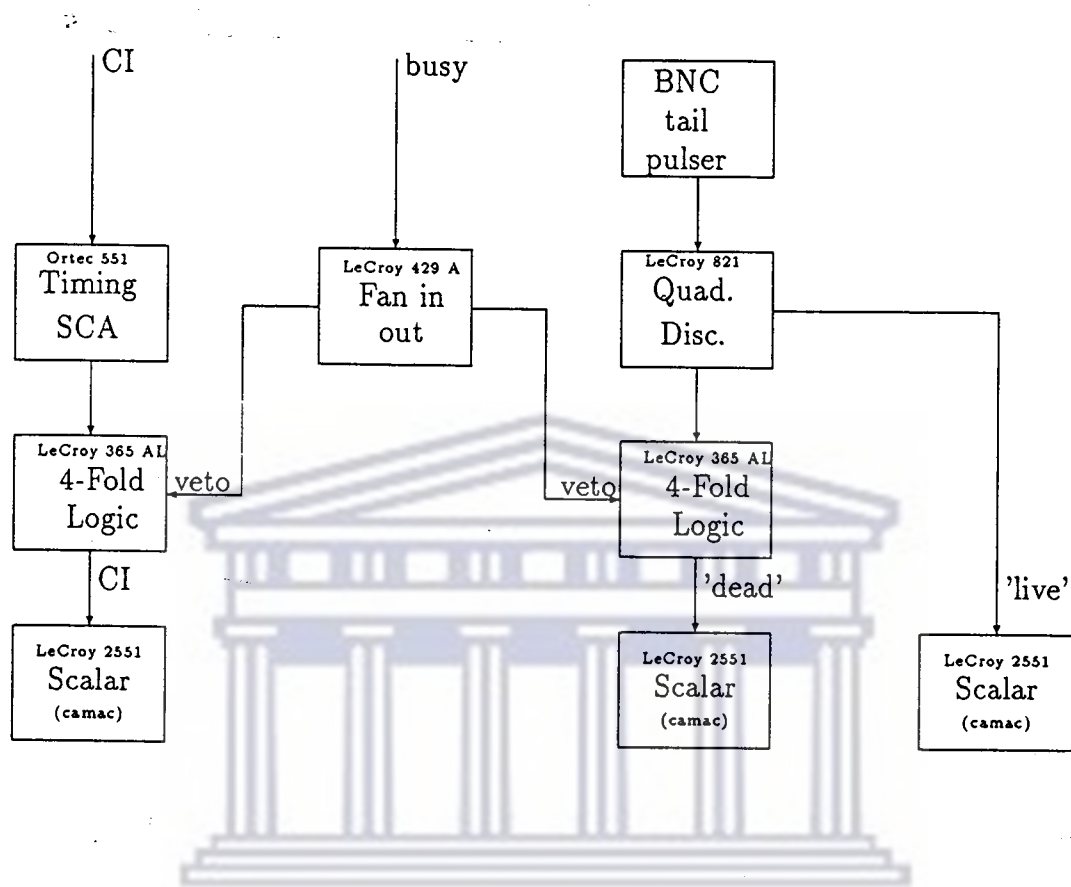
Figure 3.9: *Electronics: Dead time*

tems. During this process the event trigger module provides a busy signal which inhibits all the acquisition of event data as well as the scalar registering the accumulated charge. In order to achieve this, the current integrator (CI) output is fed through a timing Single Channel Analyzer (SCA) to convert the TTL signal to a NIM signal (see figure 3.9). This discriminated output pulse is fed through a 4-Fold-Logic unit which is vetoed by the computer busy signal. The dead time is thus automatically accounted for by using the accumulated charge in calculating the cross sections.

In order to estimate the magnitude of the dead time correction, a circuit, which

can be seen in figure 3.9, was included in the electronic set up. The signal from a BNC tail pulse generator is discriminated and fed to a scaler to record the number of pulses ('live') generated. The other output from the discriminator is fed to a 4-Fold-Logic unit along with the computer busy signal which acted as a veto. This output is sent to another scaler to record the number of pulses not vetoed ('dead') by the busy signal. The difference between the number of pulse events generated ('live') and the number of pulse events recorded in the inhibited scaler ('dead') divided by the number of pulses generated indicates the computer live time. On average the dead time was 0.8% for the ^{59}Co runs; for the ^{7}Li runs, where the event rate was higher, the dead time varied between 2 and 5%.

3.7 Data Acquisition

For on-line data acquisition a VAX-11/736 computer has been used. The interface between the electronics and the VAX-11/736 computer is a microprogrammable branch driver (MBD-11) which under the XSYS software package runs a data acquisition program (DAP) that reads data (ADC's, TDC's and scalars) from the modules in the Camac crate and sends it to the VAX-11/736 computer as events consisting of a number of data words containing ADC data, TDC data and scalar values. The software package, XSYS, has the ability of creating data areas in which the different spectra can be stored. Using the XSYS event analysis language (EVAL) a program is written to sort the event data and increment the appropriate spectra for viewing during acquisition. The event data are then written to magnetic tapes for off-line use.

Chapter 4

DATA ANALYSIS

The event data which were written to magnetic tape were subsequently analyzed on the UCT VAX 6250 computer using the XSYS software package and a Fortran minimizing program called MINUIT[a]. The (p,n) project at NAC started at the beginning of 1990. The event data for ^{59}Co were collected in three sessions starting from November 1990 to June 1991. During the first session we successfully recorded the 200 MeV data at three different laboratory angles, i.e 0°, 2°, and 4°. During this session more then five hours of event data were recorded for the zero degree angle alone. During the next session in March 1991 we collected 90 MeV, 160 MeV, and 200 MeV data. However, breakthrough was observed during some of the 200 MeV runs and these event files were therefore discarded. During the last session we collected 120 MeV data. But because of the limited beam time allocated we could only record these data at zero degree scattering angle.

Analysis of the event tapes provided a measurement of the overall time resolution. We also converted the measured time-of-flight spectra to excitation energy

---

[a]MINUIT is a function minimization and error analysis program. The program was developed at CERN by F.James and M.Roos and we used the 89.12j version.

spectra, and calculated the cross sections as well as the Gamow Teller strengths observed in this reaction. In this chapter I will discuss the data reduction procedures used and discuss the results obtained.

4.1 Time-of-flight Spectra

In a time-of-flight (TOF) system, a scintillator is viewed at its ends by two PM's through light guides. When a neutron impinges on the scintillator, it gives rise to a scintillation pulse. Let t_1 and t_2 be the times at which the two PM's give their signal. These times are recorded by the TDC's which were coupled to each PM. As discussed in the previous chapter, the PSRF supplied the time at which the particles started their flight. The position at which the particle impinges on the scintillator is measured simply by means of the time differences, i.e. t_1-t_2, and the TOF by the mean time, i.e. $(t_1+t_2)/2$.

The TOF spectra were obtained by binning these mean times event-by-event where each bin ~ 0.25ns. The TDC's were calibrated using a pulser and a variable time delay box and the times were subsequently normalized so that 4 bins = 1 ns. These normalizations was done during the off- line analysis by using a Fortran Program called GETEVENT[b]. By using the same computer program neutron data were extracted from the recorded events and then stored into a separate file for further analysis. Shown in figure 4.1-4.4 are the neutron mean time spectrum at 0° scattering angle, for $E_p = 90$, 120, 160, and 200 MeV respectively, without the subtraction of any background.

---

[b]program by D.Steyn(U.C.T)
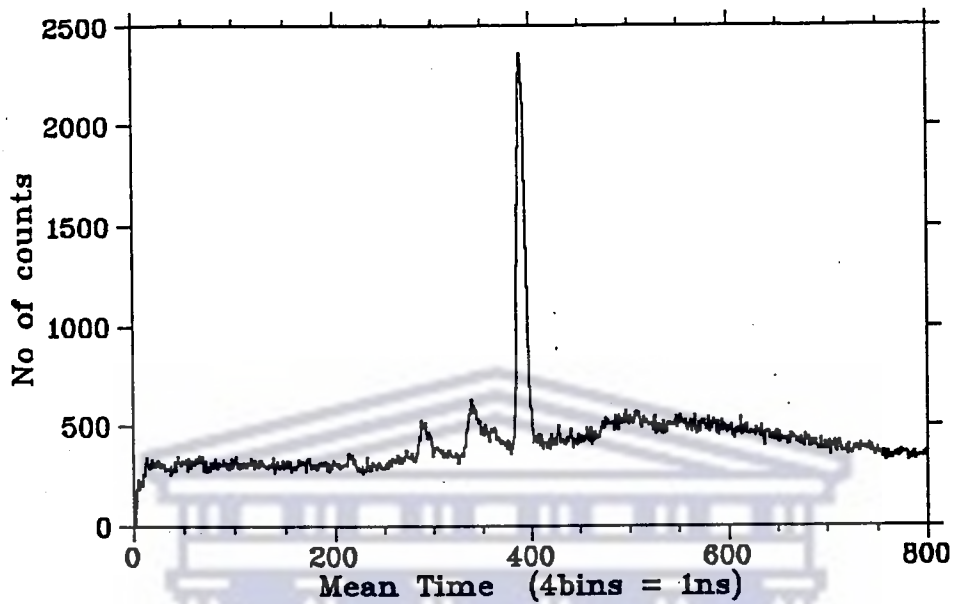
Figure 4.1: *Mean-time spectrum:* $^{59}Co(p,n)^{59}Ni$, $E_p=90$ *MeV*, $\Theta_{lab} = 0°$
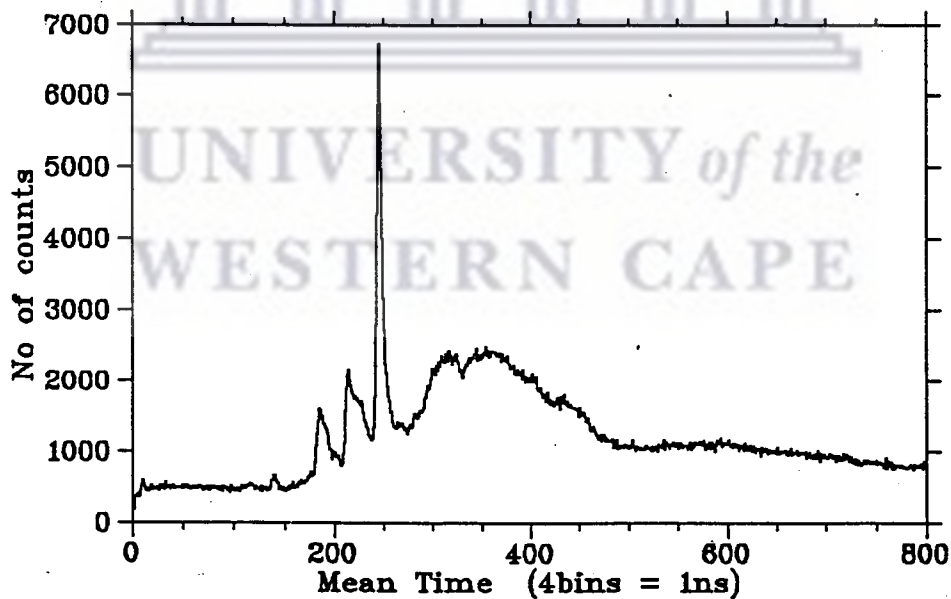
Figure 4.2: *Mean-time spectrum:* $^{59}Co(p,n)^{59}Ni$, $E_p=120$ *MeV*, $\Theta_{lab} = 0°$
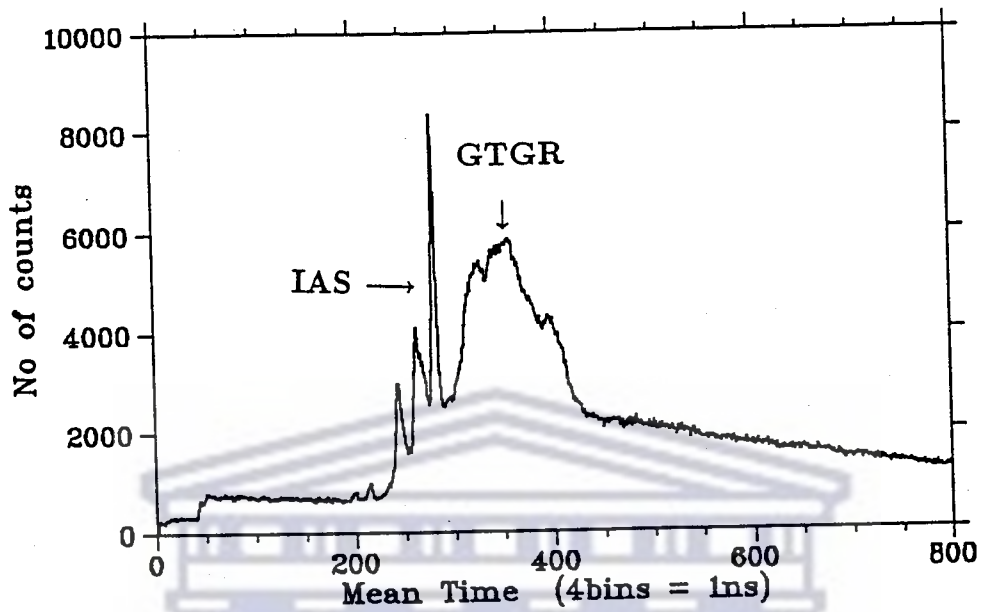
Figure 4.3: *Mean-time spectrum:* $^{59}Co(p,n)^{59}Ni$, E_p=160 MeV, Θ_{lab} = 0°
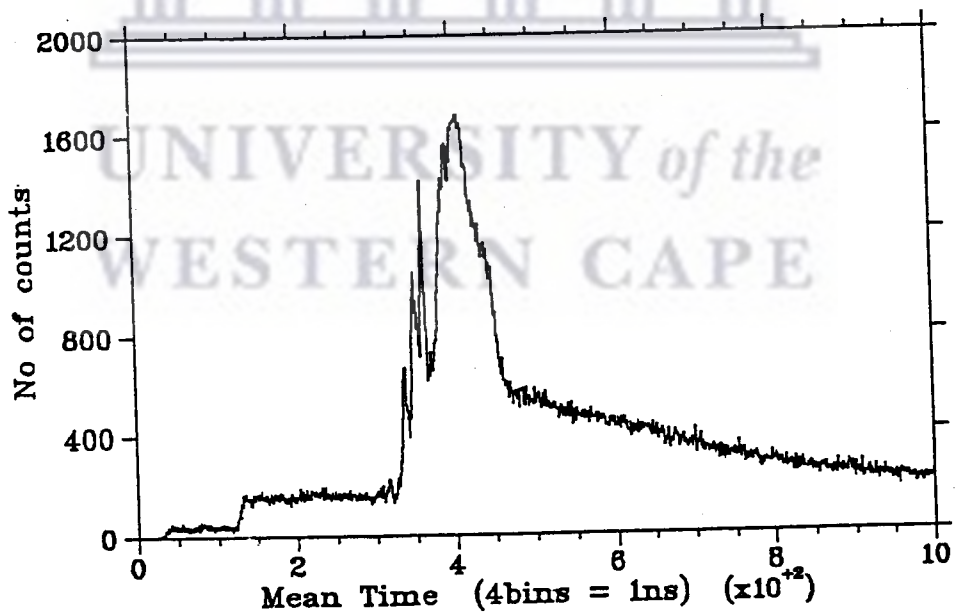
Figure 4.4: *Mean-time spectrum:* $^{59}Co(p,n)^{59}Ni$, E_p=200 MeV, Θ_{lab} = 0°

The main features of these spectra are:

- a dominant narrow peak resulting from the excitation of the $\frac{7}{2}^-$ isobaric analogue state (IAS) transition;

- a large broad bump at a later time than the IAS from the excitation of the Gamow-Teller giant resonance (GTGR);

- three/four narrow peaks at an earlier time than the IAS (the first narrow peak is identified to be the first excited state resulting from the $\frac{5}{2}^-$ GT transition); and

- the continuum region.

4.2   Overall Time Resolution

To resolve as many as possible peaks in a mean time spectrum, it is important to achieve a reasonable overall time resolution. Therefore, it is important to know what factors contributes to the overall time resolution of the neutron time-of-flight spectrometer and minimize these factors as much as possible. The factors which contribute to the overall time resolution [Mad89] of the spectrometer are estimated to be:

1. the intrinsic time resolutions of the detectors;

2. the dispersion in the timing signal obtained from the cyclotron pulse selected radio frequency (i.e, the beam burst width);

3. the nominal beam energy spread;

4. the time dispersion due to the finite target thickness; and

E_p (MeV)	90	120	160	200
run no.'s	436, 451	615	474, 476	237, 239
intrinsic time resolution (ps)	308	407	350	448
beam burst width (ps)	470	1100	850	600
beam energy spread (50keV)(ps)	707	447	284	196
finite detector thickness (ps)	822	762	647	592
target energy loss (ps)	1687	1067	443	274

Table 4.1: *Factors contributing to overall time resolution. These values are FWHM.*

5. the time dispersion due to the neutron transit time across the effective thickness of the detector.

The overall time resolution is then taken to be a quadrature sum of the five factors contributing to it.

Listed in Table 4.1 are the values obtained for the different factors contributing to the overall time dispersion. Tabulated in Table 4.2 are the values of the overall time resolution achieved during the different experimental runs as well as the calculated overall time resolution. These quoted numbers for the overall time resolution achieved are the full width at half maximum (FWHM) of the IAS in the neutron mean-time spectra.

The procedure to measure the intrinsic time resolution of the detectors is described in detail by R.Kabutz (U.C.T) in his Honours project [Kab90]. In short, cosmic events were extracted from the event data by using the Fortran program GETEVENT. By making use of the fact that cosmic rays transverse the six detectors in a straight line, and using the observed positions where the cosmic rays hit the detectors, eight parameters (two for the straight line and the six offsets

E_p (MeV)	90	120	160	200
run no.'s	436, 451	615	474, 476	237, 239
overall time resolution (ps) (calculated)	1053	1311	988	796
overall time resolution (ps) (measured)	2123	1540	1425	1493
overall energy resolution (keV) (calculated)	132	248	281	308
overall energy resolution (keV) (measured)	266	291	405	578

Table 4.2: *Summary of the calculated and measured overall time resolution. Overall calculated time resolution are the quadrature combinations of the FWHM's of the factors tabulated in Table 4.1.*

of the detectors) were obtained. After fixing two of the offsets of the detectors, only six parameters remained to be minimized. The least square method and chi square minimization were then used to calculate the other six parameters. After subtracting the fitted position from the observed position plus the offset and binning these data, gaussian curves were obtained (see figure 4.5). The values quoted[c] for the intrinsic time resolution in table 4.1 are the FWHM of the fitted curve.

The beam burst width was measured by using the proton-telescope set-up (as described in the chapter 3) and the value quoted for the beam energy spread was obtained from the beam operators. The program ELOSS V1.0[d] was used to calculate the energy loss in the target. This value was then used (in combination with equation 4.4) to determine the associated time dispersions. The target- and

---

[c]see reference [Kab92]

[d]program written by Peter Jipsen(1984)

detector thickness contributions are rectangular distributions. Because of this, the respective FWHM time dispersion contributions from the target thickness and the detector thickness are devided by $(12)^{\frac{1}{2}}$ [Mad89]. The quadrature combinations of these factors yields the tabulated overall time resolutions for the respective proton energies, and is on average about 64% of the observed overall time resolution. Possible explanations for the difference in the actual and expected resolutions might be that the contributions of some of the factors were underestimated and/or other important factors must be taken into account. The factors contributing to the overall time resolution (FWHM's) are listed in table 4.1 and in table 4.2 a summary of the overall resolution is given. There is an uncertainty of about 10% in the calculated values and about 4% in the measured values. The uncertainty in the calculated values arise from the combination of the uncertainties in the different factors contributing to the overall resolution, where the intrinsic time resolution was the major contributer. The 4% uncertainty in the measured values comes from the uncertainty in width of the gaussian peak fitted to the IAS.

4.3 Excitation Energy

4.3.1 Data Reduction

From the law of energy conservation, it is found that the excitation energy (E_x) is related to the proton energy (E_p), the neutron energy (E_n), and the energy necessary for the reaction to take place (Q-value), i.e

$$E_p + Q = E_n + E_x \tag{4.1}$$

The speed v_n of a neutron can be determined [Firk79] by measuring the time t_n that it takes to travel the flight path d. The kinetic energy (E_n) of a neutron can
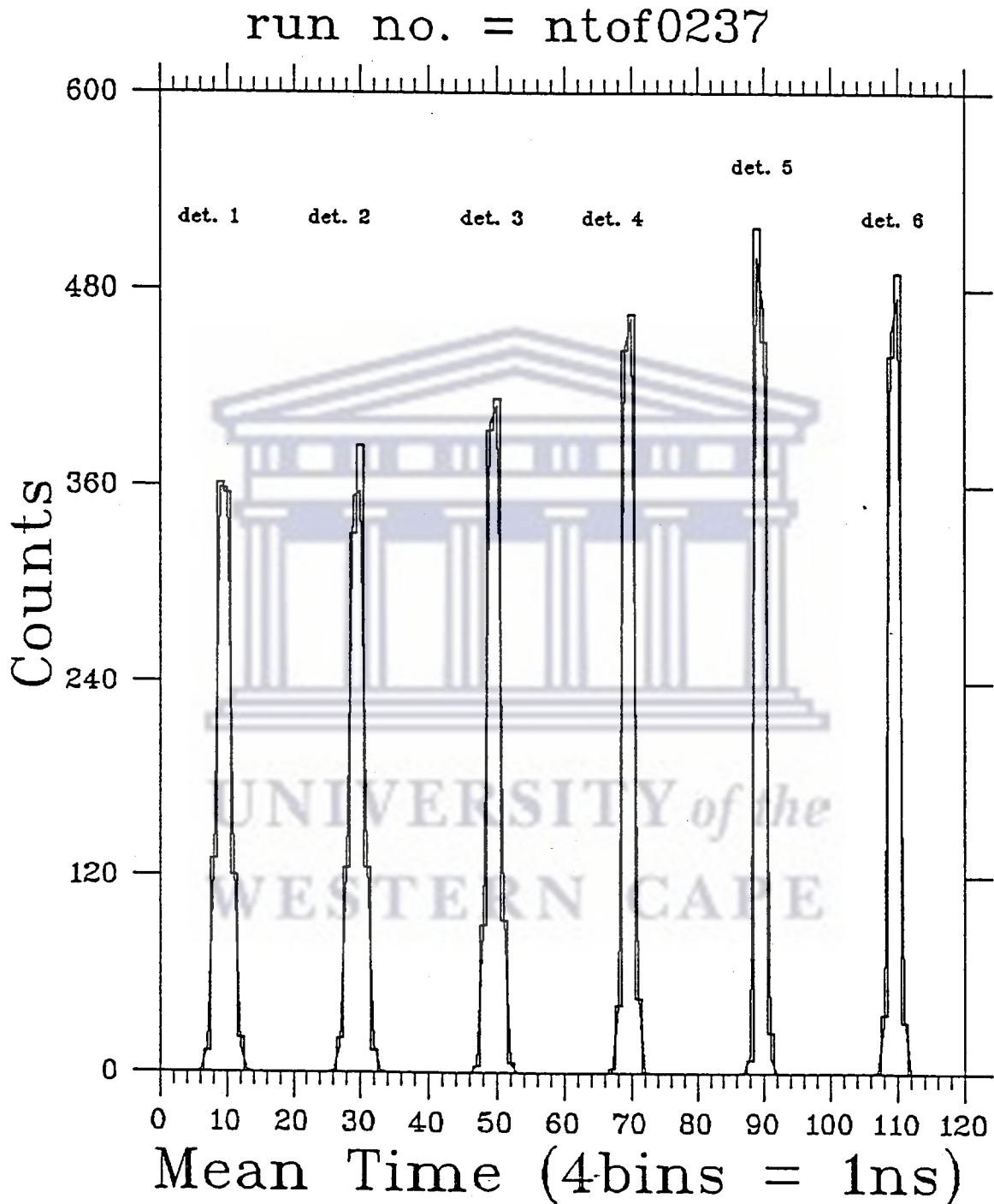
Figure 4.5: *The histograms are the observed intrinsic time resolutions of the six detectors used for run 237. The solid lines are the curves fitted to the peaks in order to determine the FWHM's*

Proton Energy (MeV)	Reference peak
90	$\frac{7}{2}^-$, IAS at $E_x = 7.18$ MeV
120	$\frac{5}{2}^-$, $E_x = 0.34$ MeV
160	$\frac{5}{2}^-$, $E_x = 0.34$ MeV
200	$\frac{7}{2}^-$, $E_x = 7.18$ MeV

Table 4.3: *Reference points used for converting the neutron time-of-flight spectra to energy spectra*

then be deduced knowing its speed, the rest energy $E_o (=939.553$ MeV) and the speed of light c, using the familiar result of special relativity:

$$E_n = E_o \left[\left(1 - \frac{v_n^2}{c^2} \right)^{-\frac{1}{2}} - 1 \right] \qquad (4.2)$$

$$E_n = E_o \left[\left(1 - \frac{d^2}{(ct_n)^2} \right)^{-\frac{1}{2}} - 1 \right]. \qquad (4.3)$$

If the units of energy are MeV, and those of length and time are m and ns respectively, then [Tay69]:

$$E_n = 939.553 \left[\left(\frac{1 - 11.126496 d^2}{t_n^2} \right)^{-\frac{1}{2}} - 1 \right] MeV \qquad (4.4)$$

The neutron time-of-flight spectra have been converted to neutron energy spectra by using $Q = -1.8556$ MeV[e] and equations 4.1 and 4.4. Discrete states in the

---

[e]see reference [Gov72]

Langsford	Anderson	This exp.	Calc.
7.05±0.14	7.14±0.09	7.18±0.10	7.34

Table 4.4: *Excitation energy of IAS (MeV).*

residual nucleus with known excitation energies were selected as reference points in the time-of-flight spectra to calibrate the energy scale. The reference points used are listed in table 4.3. Since the transformation from the mean time scale to the energy scale is non-linear, the energy spectra had to be rebinned.

4.3.2   Results and Discussion

The most recent ^{59}Co(p,n)^{59}Ni data was published by Tepel *et. al.* [f] In this paper, however, the beam energy was less than 3.3 MeV and only the level structures of ^{59}Co and other targets were studied. More useful was a paper by Langsford *et. al.* [g] where several targets were bombarded with 90 MeV protons. Although the energy resolution achieved was poor[h], peaks corresponding to the formation of the isobaric analogue states in the residual nuclei were observed in the neutron spectra. This group found that the IAS has an excitation energy of 7.05±0.14 MeV whereas Anderson *et. al.* [i] measured a value of 7.14±0.09 MeV.

In our data, we predicted[j] that the first excited state would be the first Gamow

---

[f] see reference [Tep70]

[g] see reference [Lan68]

[h] ~2 MeV (fwhm)

[i] see reference [And65]

[j] See chapter 2

Teller transition to be excited. By using the excitation energy (0.34 MeV) of this specific state to calibrate the 120 and 160 MeV energy spectra, the excitation energy of the IAS was found (see Table 4.4) to be on average equal to 7.18±0.10 MeV. This value corresponds favorably with the other published results and was used to calibrate the 90 MeV spectra, where the first excited state was not observed, and the 200 MeV spectra, where the energy resolution was not as good. The results obtained for the IAS transition are listed in Table 4.4. The calculated value was obtained from Langsford *et. al.* who used the fact that the Q-value for a transition to an IAS is given by the Coulomb displacement energy which arises from the introduction of an extra charge into the nucleus. We, therefore, established that the first peak observed in the neutron spectra indeed corresponds to the excitation of the first excited state. The excitation energy spectra obtained are plotted in figure 4.6-4.9.
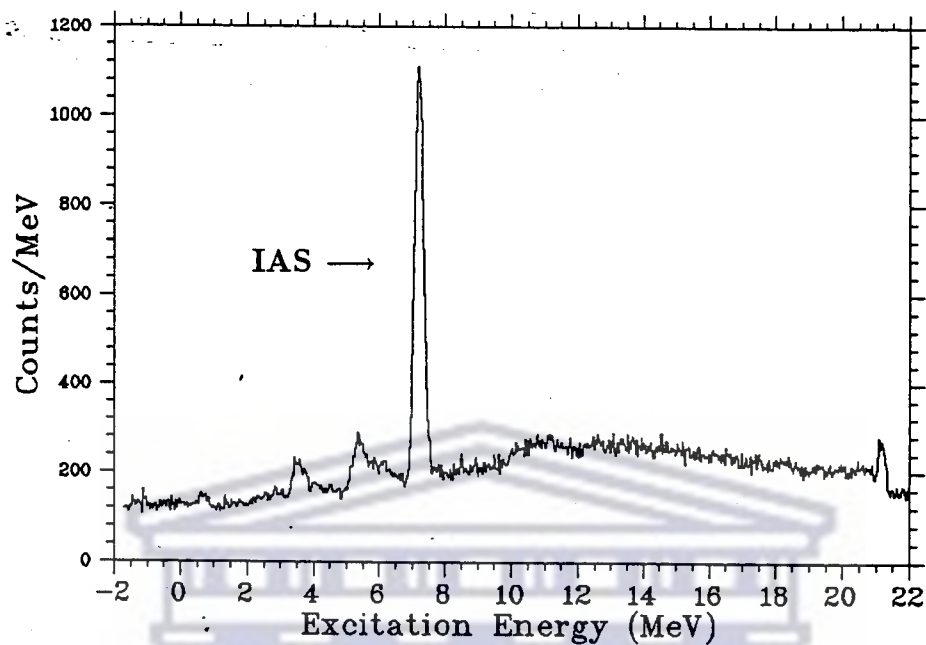
Figure 4.6: *Excitation energy spectrum:* $^{59}Co(p,n)^{59}Ni$, E_p=90 MeV, $\Theta_{lab} = 0°$
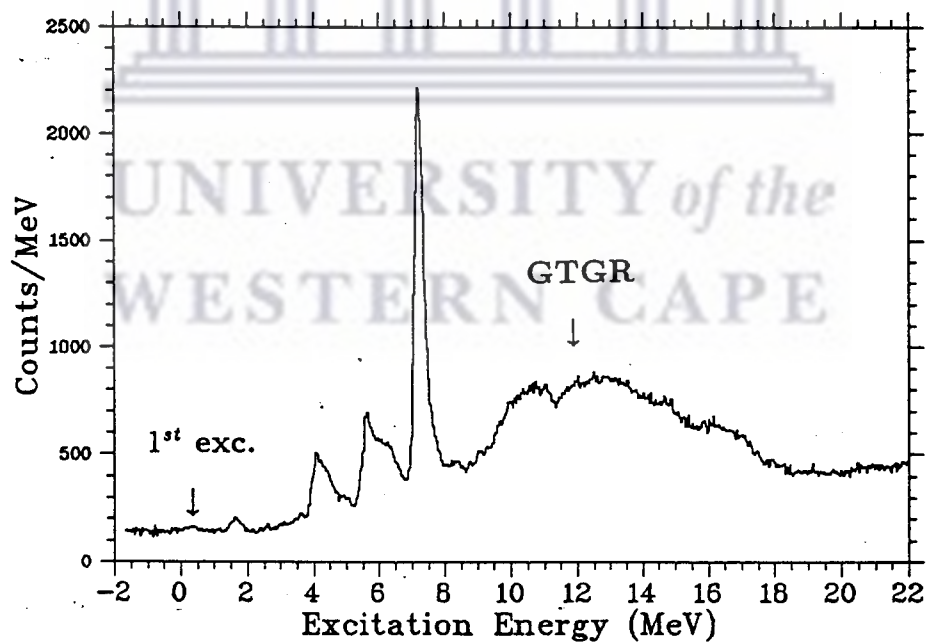
Figure 4.7: *Excitation energy spectrum:* $^{59}Co(p,n)^{59}Ni$, E_p=120 MeV, $\Theta_{lab} = 0°$
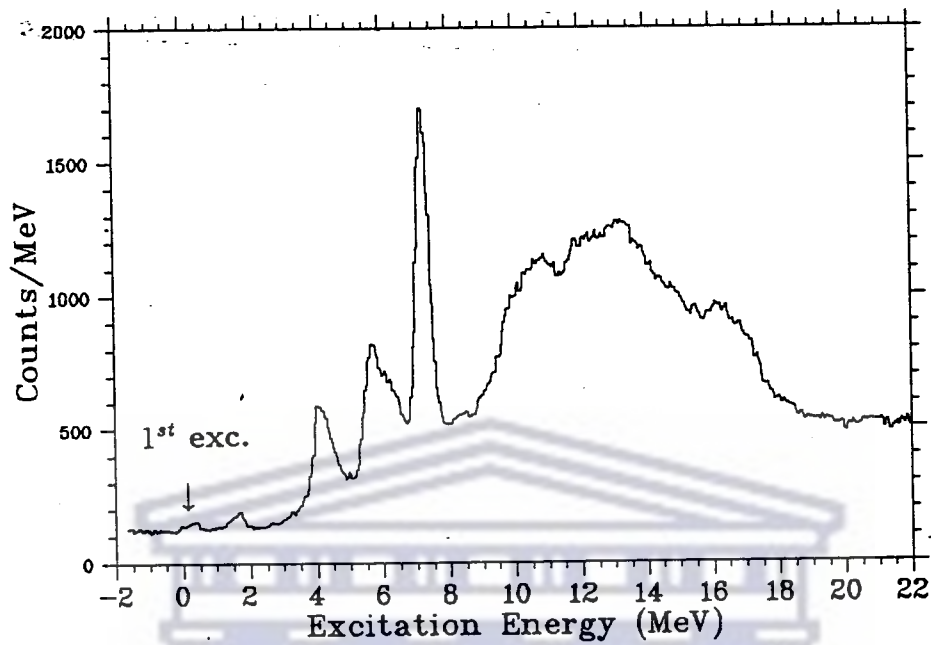
Figure 4.8: *Excitation energy spectrum:* $^{59}Co(p,n)^{59}Ni$, E_p=160 MeV, $\Theta_{lab} = 0°$
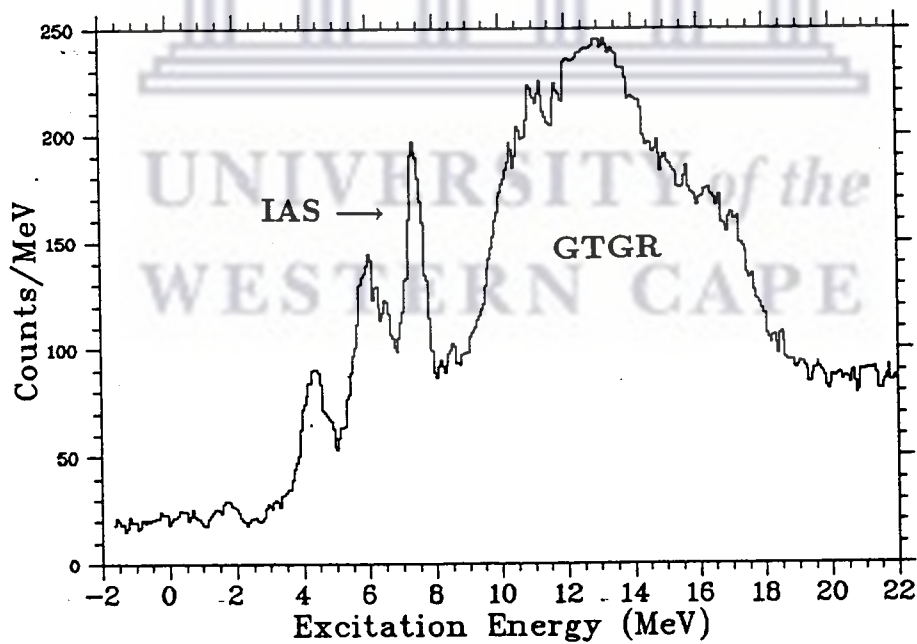
Figure 4.9: *Excitation energy spectrum:* $^{59}Co(p,n)^{59}Ni$, E_p=200 MeV, $\Theta_{lab} = 0°$

4.4   Cross Section Measurement

4.4.1   Data Reduction

The reaction cross section of the protons were determined with the following
formula:

$$\frac{d\sigma}{d\Omega} = \frac{Y}{\Delta\Omega \times I \times n \times T \times l \times \epsilon} \qquad (4.5)$$

where:

- $Y(yield)$ is the total number of counts (neutrons) per energy bin;

- $\Delta\Omega$, the solid angle subtended by the detectors [steradians];

- I, the flux of protons;

- n, the number of target nuclei per unit area [nuclei/cm^2];

- T, the fractional neutron transmission from target to detector;

- l, the fractional live time of the data acquisition system; and

- ϵ, the efficiency for detecting a neutron.

The cross sections for the individual transitions are obtained by fitting curves to
the peaks in the time-of-flight spectra. The line shape chosen for the peaks is a
symmetric Gaussian distribution of the form

$$A exp[\frac{(x-p)^2}{2\sigma^2}], \qquad (4.6)$$

where A is the amplitude, x an independent variable, p the position of the axis
of symmetry, and σ the width of the gaussian. The time-of-flight spectra were
fitted with as many peaks as the structure warranted on top of a polynomial
background. The peaks were fitted simultaneously with the background, which

was required to account for the wrap around background, the residual cosmic ray background as well as the continuum region above $\sim$18 MeV of excitation. It is plausible that part of the continuum in the spectra could be the excitation of collective states (see figure 4.10) with higher angular momenta. Therefore, we chose to defer the analysis of that region of the spectra until we have a better understanding of the continuum. Figure 4.10 displays the spectra obtained at E_p = 200 MeV for scattering angles of 2° and 4°. As the angle increases, transitions with $L > 0$ were responsible for the relative increase in yield at excitation energies of $\sim$18 MeV and above. The resonance observed at an excitation energy of about 20-28 MeV and at $\theta_{lab} = 4°$ most likely corresponds to the excitation of the $L = 1$ giant dipole resonance.

The subtraction of a background automatically introduced a systematic uncertainty. At 200 MeV proton energy this uncertainty was most pronounced and it was estimated to be $\sim$16%. The factors contributing to the overall systematic uncertainty are listed in table 4.5. Because all these peaks were fitted simultaneously, the widths of the low lying peaks were varied together with the width of the IAS since they were determined largely by instrumental factors. The widths, positions and amplitudes of the gaussians were determined from minimization of the χ^2. We used a Fortran subroutine, MINUIT, as the minimizer. The number of peaks required to fit the unresolved structures were determined subjectively. Given an overall energy resolution[k] of $\sim$400 keV and a typical level spacing in the residual nucleus of a few tens of keV, each of the fitted peaks, except for the IAS transition and a few very low-lying (first two states) transitions, most likely corresponds to an unresolved group of states.

---

[k]This value is applicable to E_p=160 MeV. See Table 4.2 for the energy resolutions obtained at the other incident energies.
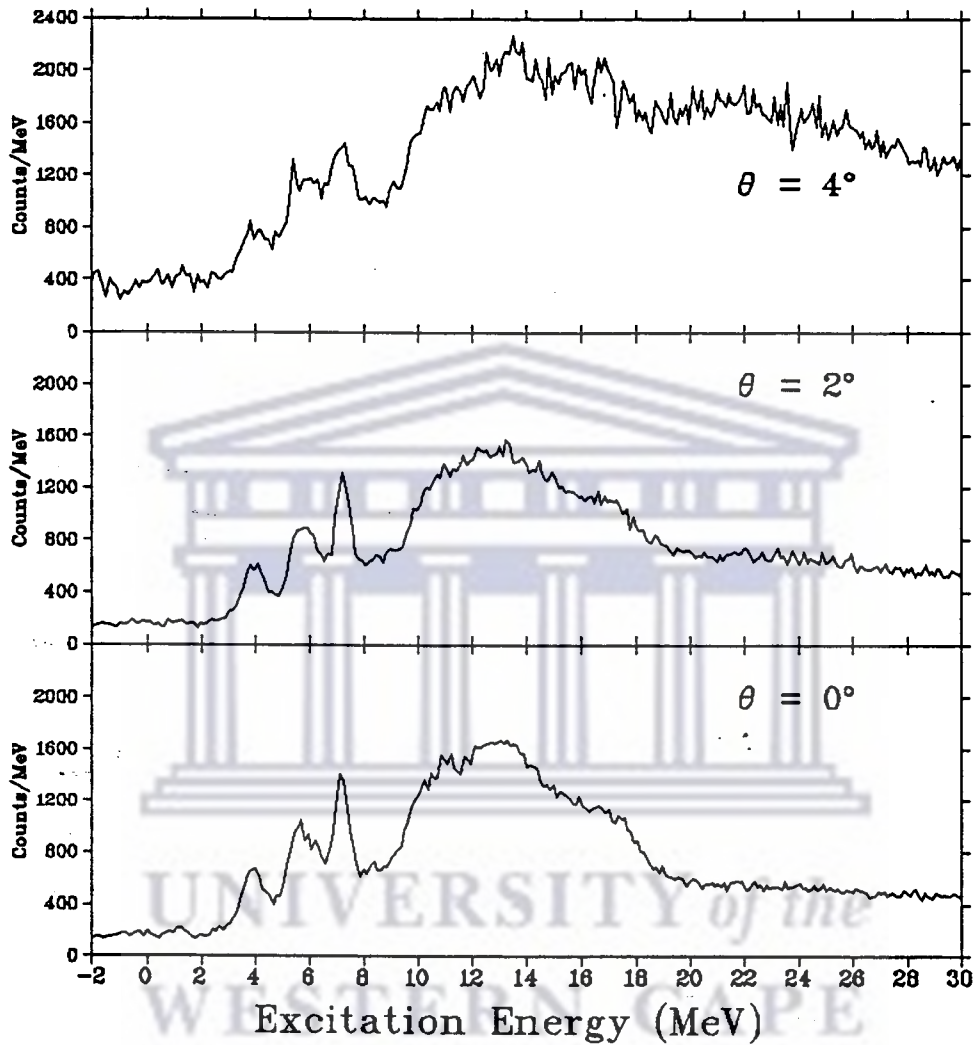
Figure 4.10: *Neutron yield versus excitation energy for the $^{59}Co(p,n)^{59}Ni$ reaction at 200 MeV and laboratory angles of 0°, 2°, and 4°. The spectra are plotted so that the peak at $E_x \approx 7.2$ MeV (the IAS) has an approximately constant amplitude.*

No. of nuclei/unit area	1.2%
Solid angle	0.1%
Efficiencies	2.6%
Charge	1%
Yield	4 - 12%
Background	8 - 16%
Overall uncertainty	< 20%

Table 4.5: *Factors contributing to the overall uncertainty in the cross sections - uncertainty in yield is fit dependent, whereas the uncertainty in background is energy dependent.*

Integrating the Gaussian form gives

$$Yield = \sigma \times A \times \sqrt{2\pi} \qquad (4.7)$$

where σ is the width and A is the amplitude of the gaussian respectively [Kra88]. The yield associated with each fitted gaussian was found using the equation above. The yields were combined with the known target density, detector solid angle, the calculated detector efficiencies [New91], and the measured beam integration to obtain the differential cross sections of the reaction. Cross sections were corrected for neutron attenuation in the air, perspex window of the detector hut, and the

aluminium container of the detector, and where necessary for system dead time[l].

The corrections mentioned above and the detector efficiencies were calculated by R.T.Newman in partial fulfillment of his M.Sc. degree. The procedure used [The Secondary Measurement Technique] to determine the efficiencies is described in detail in his thesis (see reference [New91]). In short, the efficiencies were determined by measuring the differential cross section for the $^7Li(p,n)^7Be(gs + 0.43$ MeV) reaction and comparing it with known cross sections. The weighted averages of the extracted efficiencies of two short ^{7}Li runs, which sandwiched a ^{59}Co run, was taken as the efficiency of the detectors for that specific run.

4.4.2   Results and Discussion

The time-of-flight spectra with the peak fitting results are shown in figure 4.11-4.14. The 90 MeV spectrum shown in figure 4.11 is dominated by the IAS transition while at this proton energy the Gamow-Teller transitions are not yet well structured. The first excited state is also not yet visible at this energy. A large broad bump which correspond to the excitation of the GTGR (Gamow-Teller giant resonance) can be observed. Five low-lying peaks, an IAS peak, as well as a broad peak to fit the GTGR, were fitted to this spectrum. This broad peak is most likely a combination of several unresolved peaks. In figure 4.12 the 120 MeV spectrum at 0° is plotted. Here the first excited state can be seen. The first two peaks, as well as the IAS, correspond to resolved states. Some unresolved structures can be observed at excitation energies less than ~8 MeV. Four more peaks were fitted to simulate the GTGR. The 160 MeV spectrum can be seen in

---

[l]For the earlier sessions it was necessary to correct for the system dead time but for the last few sessions an electronic circuit [see figure 3.9] was included which automatically accounted for the system dead time.
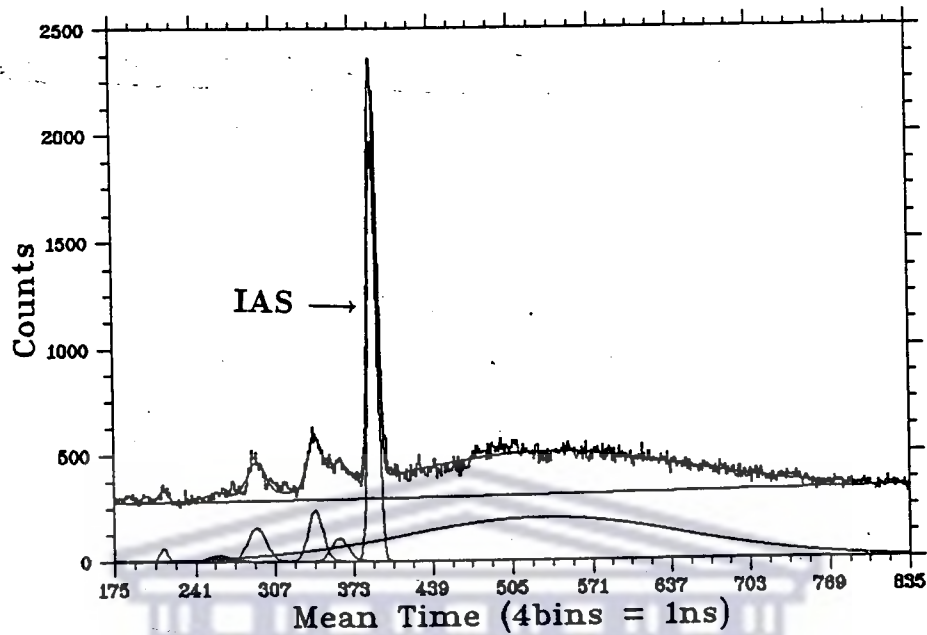
Figure 4.11: *Neutron time-of-flight spectrum: $E_p=90$ MeV, $\Theta_{lab} = 0°$. The solid lines show the peaks fitted above a linear background.*
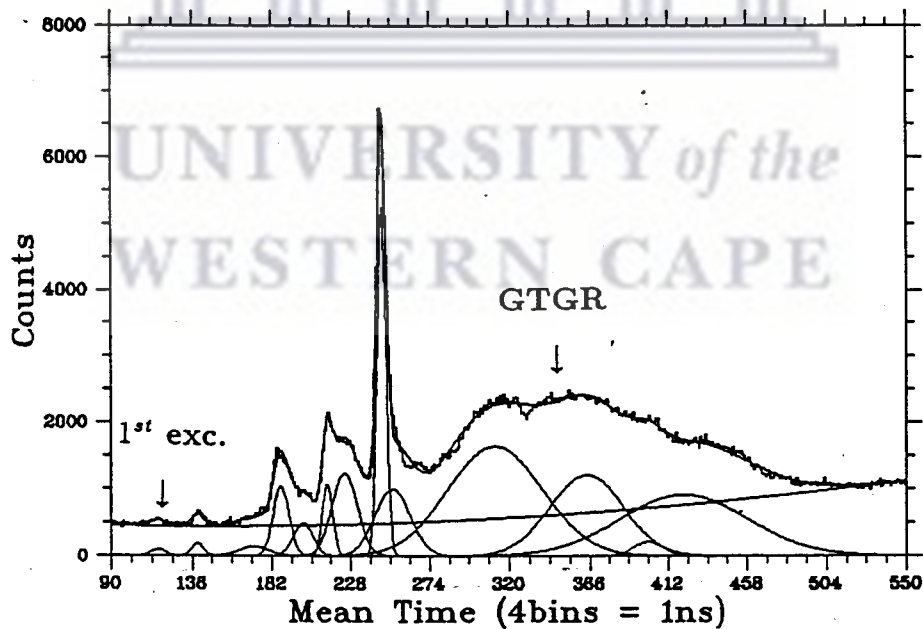
Figure 4.12: *Neutron time-of-flight spectrum: $E_p=120$ MeV, $\Theta_{lab} = 0°$. The solid lines show the peaks fitted above a quadratic background.*
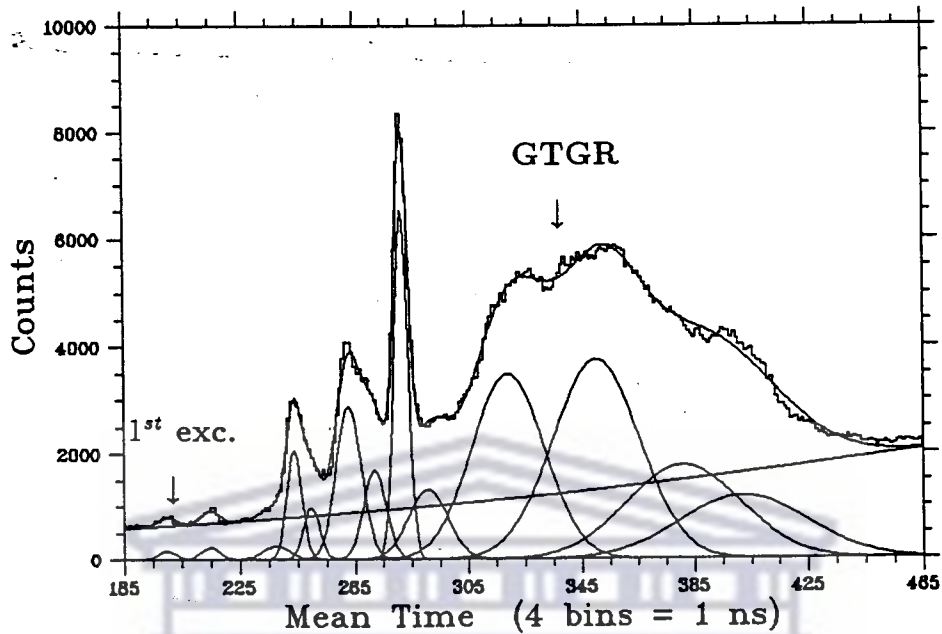
Figure 4.13: *Neutron time-of-flight spectrum: E_p=160 MeV, Θ_{lab} = 0°. The solid lines show the peaks fitted above a quadratic background.*
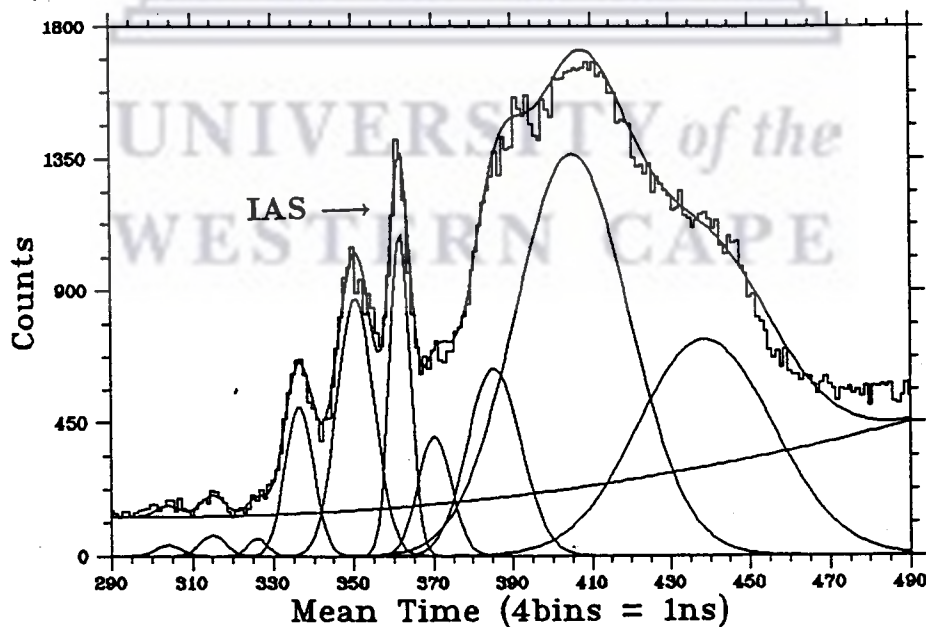
Figure 4.14: *Neutron time-of-flight spectrum: E_p=200 MeV, Θ_{lab} = 0°. The solid lines show the peaks fitted above a quadratic background.*

figure 4.13. Apart from the resolved states and the IAS, six peaks were used to fit the unresolved structures at low excitation energy, and four peaks to fit the GTGR. At 200 MeV the energy resolution was not as good as for the lower proton energies and it was therefore easier to fit one peak to an unresolved structure as can be seen in figure 4.14.

The differential cross sections for the peaks observed at 0° from the (p,n) reactions on ^{59}Co are listed in Tables 4.8-4.9. The differential cross sections for the IAS and the GTGR are plotted in figure 4.15 and 4.16 respectively.

4.5   Gamow-Teller Strength

4.5.1   Data Reduction

From equation 2.9, it is evident that the 0° (p,n) cross section is proportional to $B(GT)$. The proportionality can be determined by measuring the 0° cross section for a transition with known β decay. Unfortunately, such a convenient reference transition was not available for ^{59}Co and an alternative method had to be found.

From the Fermi and GT selection rules listed in Table 2.1 it is evident that the IAS is a pure Fermi state if the transition is $0^+ \rightarrow 0^+$, and a GT mixed transition if $\Delta S = 0, \pm 1$ and $S \neq 0$ as can be seen in odd-mass nuclei. In order to extract B(GT) values for ^{59}Co, we needed to know the relative strengths of the GT to Fermi transitions. Using the fact that for such transitions, the cross sections at 0° is the incoherent sum of the Fermi and GT pieces, Taddeucci and his collaborators has found that the fraction of the cross sections attributable to the GT or Fermi
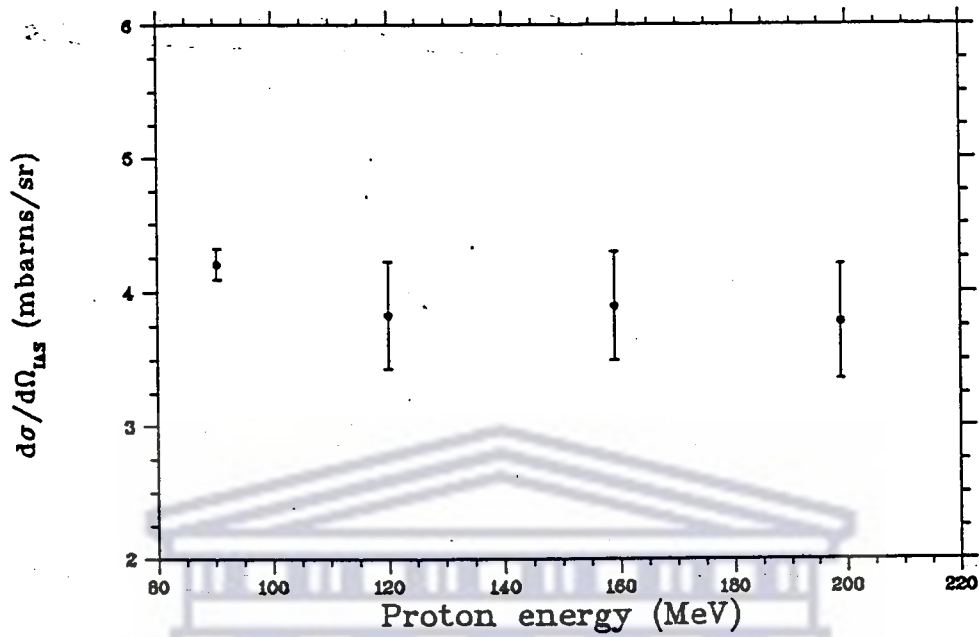
Figure 4.15: *Laboratory differential cross sections associated with the IAS in the* $^{59}Co(p,n)^{59}Ni$ *reaction at zero degree scattering angle as a function of proton energy.*
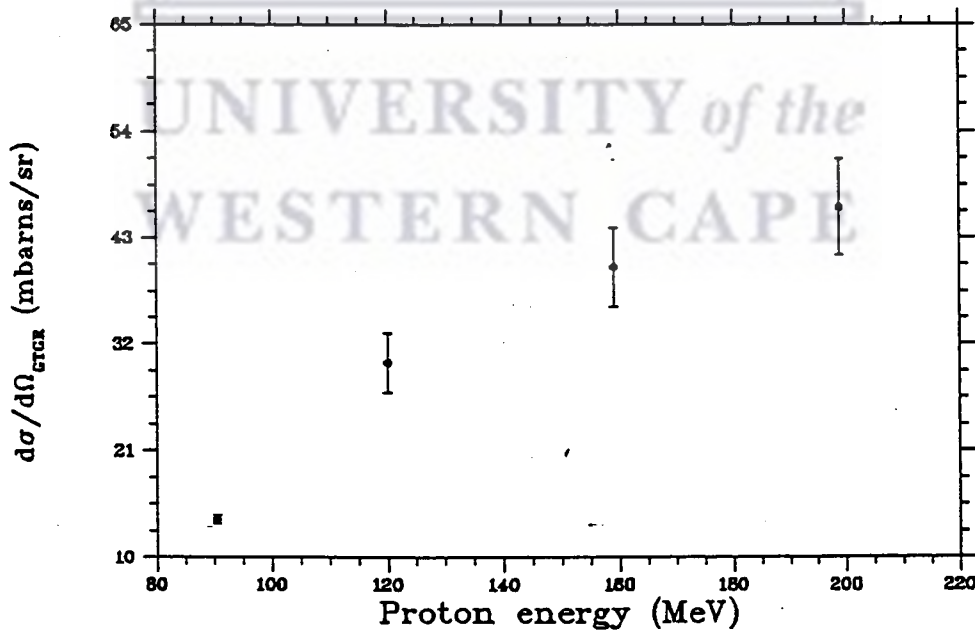
Figure 4.16: *Laboratory differential cross sections associated with the GTGR in the* $^{59}Co(p,n)^{59}Ni$ *reaction at zero degree scattering angle as a function of proton energy.*
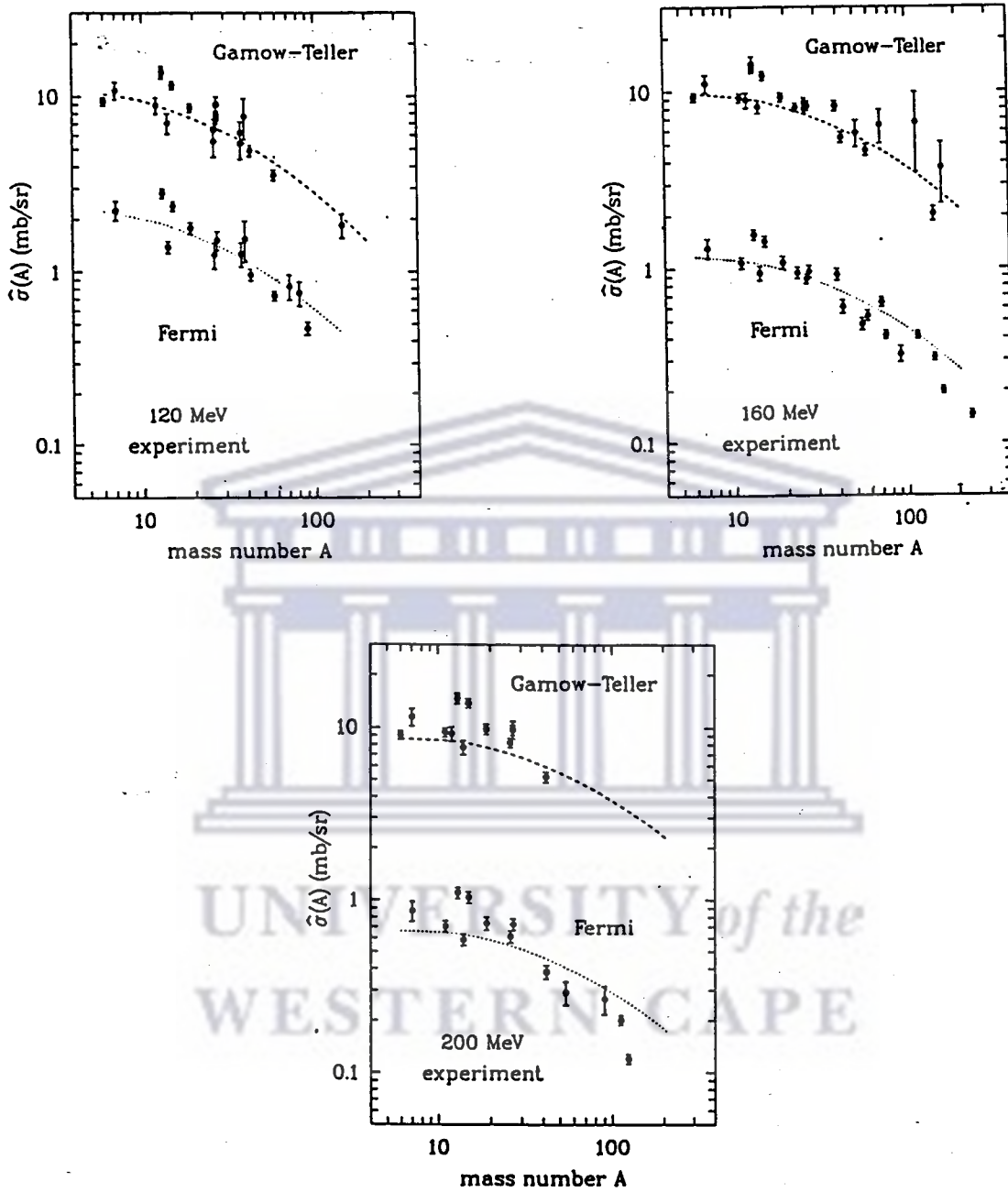
Figure 4.17: *Experimental unit cross sections for Gamow-Teller and Fermi transitions at E_p = 120, 160, and 200 MeV. The dashed line is the DWIA calculation. See reference [Tad87].*

E_p(MeV)	120	160	200
$\hat{\sigma}_{GT}$(mb/sr)	3.9±0.5	5.1±0.6	5.1±0.8
$\hat{\sigma}_F$(mb/sr)	0.74±0.15	0.63±0.09	0.36±0.08
R^2	5.27±1.26	8.10±0.61	14.17±0.80

Table 4.6: *Unit cross sections extracted from figure 4.17.*

strength is given by

$$f_{GT} = 1 - f_F = \frac{\sigma_{GT}}{\sigma_{IAS}} = \left[1 + \frac{B(F)}{B(GT)R^2}\right]^{-1}, \qquad (4.8)$$

where R^2 represents the ratio of unit cross sections as defined in chapter 2.

By making use of the assumption that the momentum transfer (q) is limited to zero at 0° cross section measurements, the proportionality factor (see equation 2.18) can then be given as

$$\hat{\sigma}_{GT} = f_{GT} \frac{\sigma(0°)}{B(GT)} \qquad (4.9)$$

The empirical results for unit cross section are plotted for $E_p = 120$, 160, and 200 MeV in figure 4.17. Taddeucci *et. al.* [Tadd87] used the DWIA theory to calculate these unit cross sections (the dashed line) for comparison with known experimental results. These plots were used to extract the unit cross sections (see Table 4.6) as well as the ratio $\hat{\sigma}_{GT}/\hat{\sigma}_F$ for $A \sim 59$. These values were then used to calculate the transition strengths in the other observed peaks and to calculate the f_{GT} values. This, however, introduced large uncertainties.

For the 90 MeV data set another procedure had to be used to determine the GT strength distribution since the unit cross sections were not available. After thorough investigation, we have decided to use the empirical value of R^2 and the average of the calculated GT strengths observed in the peak at $E_x \sim 4$ MeV in the 120 MeV and 160 MeV spectra to accomplish our objective. The decision to use these data sets was motivated by the superior energy resolution achieved at these beam energies. On average the $B(GT)^-_{\sim 4MeV} = 0.297 \pm 0.065$ and from equation 2.16, it follows that $R^2 = 4.00 \pm 0.03$.

4.5.2   Nuclear Shell-Model Calculations

In many areas of science models are used to simplify the understanding of complex processes. The merit of any model is evaluated in terms of its capacity to reproduce experimentally known properties of nuclei. One dominant model used today in describing the energy levels of nuclei, magnetic dipole and quadrupole moments, spectroscopic factors, B(E2) and B(M1) transition rates, log ft values and Gamow-Teller strengths and distributions, is the Shell-Model [Kra88].

Assuming that in a system of A particles, N of these particles might arrange themselves into a closed shell and an inert core, and that the effective Hamiltonian acts only on a model-subspace of the complete nuclear space, the number of orbitals being populated can be reduced to a small finite number.

In this section a cryptic explanation will follow of the procedures used by van der Merwe *et. al.* to determine the Gamow-Teller strength distributions of the nucleus under investigation. Readers are referred to [Van92] for additional information.

The energies of a nucleus are determined by solving the eigenvalue problem for the Hamiltonian

$$H\Phi = E\Phi, \tag{4.10}$$

with

$$H = H_{core} + V_c + H_{sm}, \tag{4.11}$$

where

- H_{core} denotes the Hamiltonian in the inactive core, and

- V_c is the Coulomb interactions between the protons.

From [Bro88] it can be seen that the matrix elements of the shell-model Hamiltonian can be expressed in terms of a summation over the products of the one-body transition density, OBTD, with the single-particle energy, SPE, plus the product of the two-body transition density, TBTD, with the two-body matrix elements, TBME, i.e:

$$H_{sm} = h_{sm} + \nu_{eff}, = \sum_i \epsilon_i^{sm} a_i^+ a_i + \frac{1}{4} \sum_{ijkl} < ij|\nu_{eff}|kl > a_i^+ a_j^+ a_l a_k \tag{4.12}$$

where

- h_{sm} and ν_{eff} are the single particle Hamiltonian and the effective interaction for the valence nucleons respectively;

- $< ij|\nu_{eff}|kl >$, the TBME;

- a^+ and a the creation and annihilation operators; and

- $\sum_{ijkl}$, the sum over the indices labelling the single-particle states.

Various approaches, such as the empirical, semi-empirical, and Linear Combinations (LC) method, could have been followed to determine the matrix elements,

but van der Merwe and collaborators [Van92] found the LC method to be the most efficient and reliable option in this mass region. The difficulties encountered with the empirical approach was the large number of TBME which made it impossible to employ. The semi-empirical method proved to be too expensive on CPU time (350 hours CPU time on the SUNVAX) and the spin-orbit and tensor terms were found too large.

With the LC method it is possible to identify which particular combinations of parameters are most important to reproduce the experimental energies. In a fit to experimental data only the well determined linear combinations of parameters need then be varied to reproduce the experimental spectra, while the poorly determined ones can be fixed at predetermined theoretical values.

A model space consisting of $0f_{\frac{7}{2}}^{n}(1p_{\frac{3}{2}}0f_{\frac{5}{2}}1p_{\frac{1}{2}})^{m} + 0f_{\frac{7}{2}}^{n-1}(1p_{\frac{3}{2}}0f_{\frac{5}{2}}1p_{\frac{1}{2}})^{1+m}$, with m the number of nucleons outside the $\frac{7}{2}$ shell, was considered. The ^{40}Ca core was assumed to be inert. A total of 177 parameters was considered. The forty best-determined linear combinations out of this set of parameters were then allowed to vary while the remaining ones were fixed at the FPVLB3 starting interaction (see reference [Van92]). The FPVLB3 starting interaction was obtained from the LC study of a model space that allowed the excitation of only one particle to the $(p_{\frac{3}{2}}, f_{\frac{5}{2}}, p_{\frac{1}{2}})$ shell.

4.5.3   Results and Discussion

The model independent sum rule is restricted to nuclei where both $B(GT)^{-}$ and $B(GT)^{+}$ are known. In the present case, however, an upper limit for the observed GT strength can be obtained, by putting $\sum B(GT)^{+} = 0$. This is acceptable since with the large neutron excess, the β^{+} decay is practically blocked by the Pauli

	E_p(MeV)	90	120	160	200	Shell-Model
(a)	$\sum B(GT)^-$	7.21±1.29	10.09±0.76	9.68±0.62	11.11±1.18	9.09
(b)	Sum Rule	48%	67%	65%	74%	61%
(c)	f_{GT}	0.28±0.06	0.04±0.01	0.19±0.04	0.29±0.07	-

Table 4.7: *Tabulated are: (a) the total GT strength experimentally observed, and the theoretical value obtained from Shell-Model calculations, (b) the percentage of the observed GT strength as predicted by the Sum Rule, and (c) the fraction of the GT strength in the IAS.*

principle.

A summary of the results can be seen in Table 4.7. The $B(GT)$ value for each GT transition was calculated using equation 4.9. Equation 4.8, in conjunction with equation 2.19, was used to calculate the fraction of the GT strength situated in the mixed IAS transition. The rather large uncertainties (up to about 25%) in the results emanate directly from the procedures used to extract these values. Since f_{GT} is directly proportional (see equation 4.8) to R^2 the discrepancies in these values could also be ascribed to this and to the fact that in the plots (see figure 4.17) used to extract the unit cross sections, no distinction was made between odd-mass and even-mass nuclei. This destinction is, however, necessary as can be concluded from equations 2.15 and 2.16 and also from the most recent polarization transfer measurements (see reference [Hua91]). The large value of f_{GT} at $E_p = 90$ MeV could be ascribed to the fact that we have used the emperical

formula (equation 2.16) to calculate R^2. The sharp increase in f_{GT} at the other bombarding energies, i.e 120, 160, and 200 MeV, is expected since f_{GT} is directly proportional to E_p^2. The GT strengths obtained during this experiment are listed in Tables 4.8 - 4.9, and are graphically depicted in figures 4.18 - 4.21. The Shell-Model calculation predicts GT strength in the region $8.00 \leq E_x(MeV) \leq 20$ (see figure 4.22). This, however, corresponds to the excitation of the GTGR.
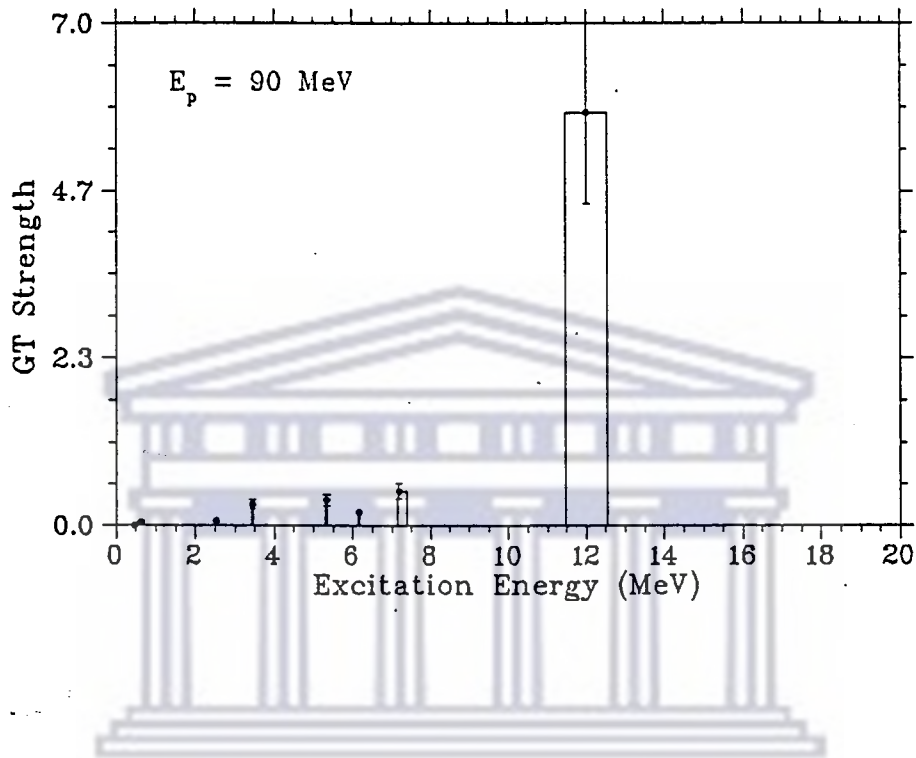
Figure 4.18: *Gamow-Teller strength distribution: $E_p=90$ MeV. The histograms represents the location of the peaks identified in Figure 4.11. The width of the histograms corresponds to the uncertainties in the excitation energies observed. The histograms up to $E_x \sim 7.5$ MeV represents single transitions, while the histogram at higher excitation energy represents the approximate location of the unresolved GTGR.*

Figure 4.19: *Gamow-Teller strength distribution: $E_p=120$ MeV. The histograms represents the location of the peaks identified in Figure 4.12. The width of the histograms corresponds to the uncertainties in the excitation energies observed. The histograms up to $E_x \sim 7.5$ MeV represents single transitions, while the histograms at higher excitation energy represents the approximate location of the unresolved GTGR.*

Figure 4.20: *Gamow-Teller strength distribution: E_p=160 MeV. The histograms represents the location of the peaks identified in Figure 4.13. The width of the histograms corresponds to the uncertainties in the excitation energies observed. The histograms up to $E_x \sim 3.5$ MeV represents single transitions, while the histograms at higher excitation energy represents the approximate location of the unresolved states as well as the GTGR.*

Figure 4.21: *Gamow-Teller strength distribution: E_p=200 MeV. The histograms represents the location of the peaks identified in Figure 4.14. The width of the histograms corresponds to the uncertainties in the excitation energies observed. The histograms up to $E_x \sim 3.5$ MeV represents single transitions, while the histograms at higher excitation energy represents the approximate location of the unresolved states as well as the GTGR.*
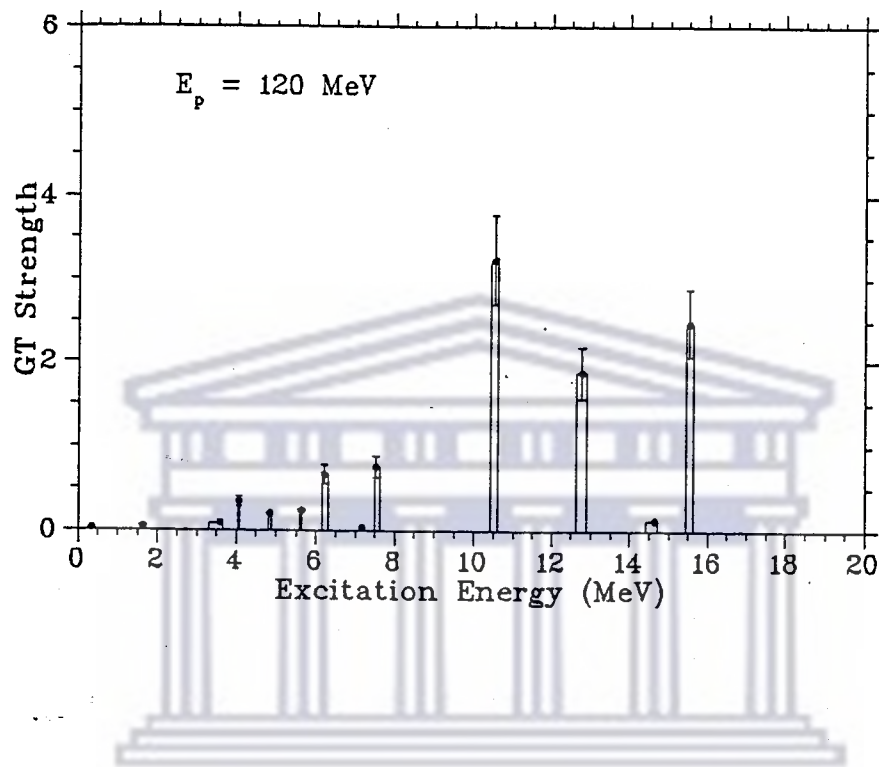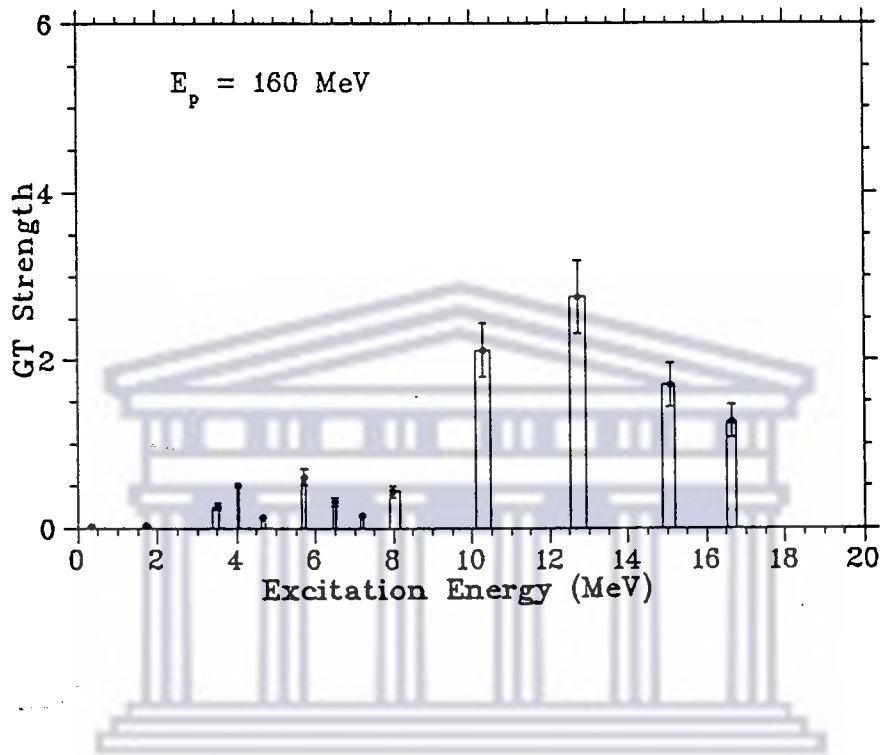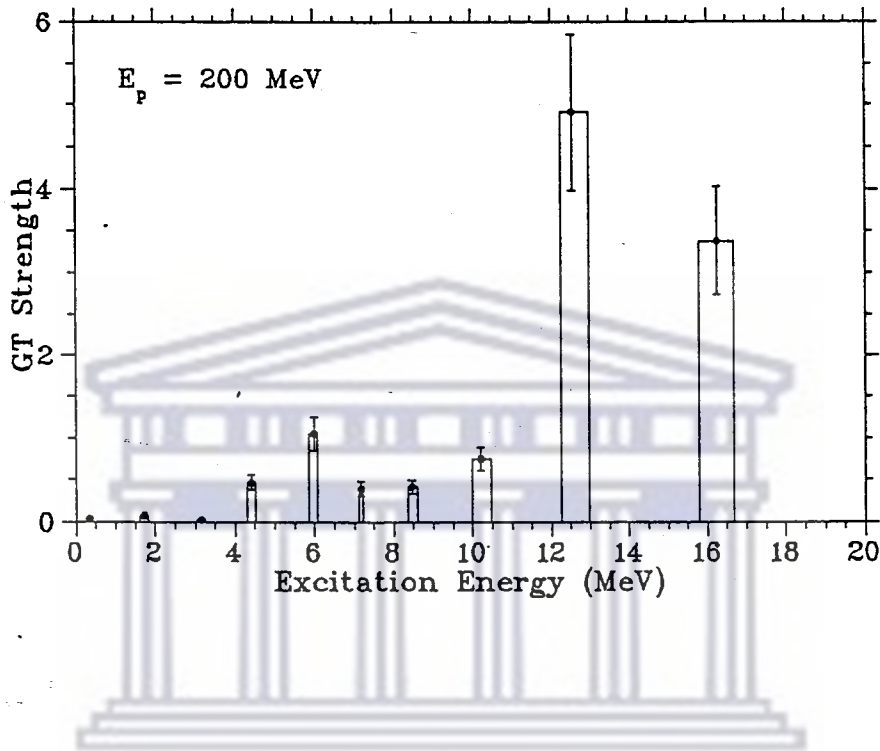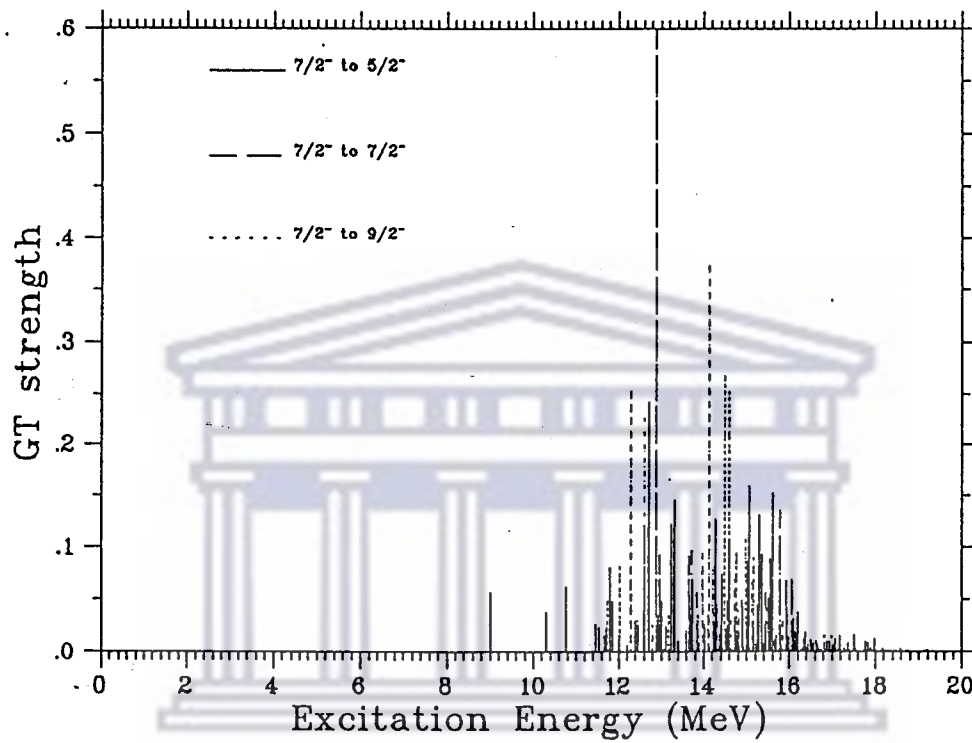
Figure 4.22: *Gamow-Teller strength distribution: Shell-Model calculations. Note the difference in scales between this plot and the previous plots.*

Proton energy (MeV)	Excitation energy (MeV)		Cross sections (mb/sr)		GT strength	
E_p	E_x	$\triangle E_x$	σ	$\triangle \sigma$	GT	$\triangle GT$
90	0.45	0.09	0.018	0.018	-	-
	0.61	0.09	0.112	0.008	0.046	0.011
	2.52	0.06	0.153	0.011	0.064	0.015
	3.44	0.04	0.711	0.020	0.297	0.065
	5.33	0.04	0.867	0.034	0.362	0.081
	6.16	0.06	0.442	0.022	0.185	0.042
	7.18†	0.09	4.208	0.114	0.49	0.11
	12.00	0.22	13.804	0.398	5.768	1.283
120	0.34	-	0.114	0.015	0.029	0.006
	1.63	0.08	0.186	0.022	0.048	0.011
	3.58	0.27	0.352	0.038	0.090	0.015
	4.06	0.08	1.354	0.143	0.347	0.057
	4.85	0.12	0.795	0.085	0.204	0.034
	5.63	0.08	0.916	0.100	0.235	0.040
	6.20	0.21	2.597	0.270	0.667	0.110
	7.17†	0.08	3.833	0.395	0.04	0.01
	7.55	0.08	2.964	0.306	0.760	0.125
	10.51	0.08	12.616	1.297	3.235	0.532
	12.98	0.12	7.309	0.752	1.874	0.308
	14.63	0.21	0.511	0.053	0.131	0.022
	15.53	0.21	9.650	0.992	2.474	0.407

Table 4.8: *The differential cross sections for the peaks observed at 0° scattering angle and at 90 and 120 MeV proton energies. The isobaric analogue state (IAS) is indicated by the dagger, †.*

Proton energy (MeV)	Excitation energy (MeV)		Cross sections (mb/sr)		GT strength	
E_p	E_x	$\triangle E_x$	σ	$\triangle \sigma$	GT	$\triangle GT$
160	0.34	-	0.117	0.015	0.023	0.004
	1.71	0.12	0.176	0.021	0.035	0.006
	3.52	0.16	1.309	0.162	0.057	0.011
	4.03	0.12	0.290	0.046	0.257	0.044
	4.66	0.13	0.663	0.104	0.130	0.025
	5.71	0.12	3.105	0.327	0.609	0.096
	6.49	0.13	1.616	0.171	0.317	0.050
	7.19†	0.12	3.895	0.401	0.148	0.026
	7.97	0.16	2.227	0.231	0.437	0.069
	10.29	0.16	10.818	1.113	2.121	0.324
	12.72	0.16	14.051	1.445	2.755	0.430
	15.08	0.16	8.670	0.891	1.700	0.266
	16.64	0.16	6.440	0.662	1.263	0.197
200	0.34	0.09	0.174	0.020	0.034	0.007
	1.73	0.16	0.389	0.053	0.076	0.016
	3.16	0.16	0.147	0.018	0.029	0.006
	4.40	0.16	2.353	0.262	0.461	0.089
	5.99	0.16	5.348	0.576	1.049	0.200
	7.18†	0.09	3.782	0.426	0.387	0.090
	8.45	0.16	2.110	0.239	0.414	0.080
	10.21	0.24	3.793	0.399	0.744	0.141
	12.53	0.24	25.091	2.675	4.920	0.933
	16.24	0.24	17.253	1.944	3.383	0.653

Table 4.9: *The differential cross sections for the peaks observed at 0° scattering angle and at 160 and 200 MeV proton energies. The isobaric analogue state (IAS) is indicated by the dagger, †.*

Chapter 5

CONCLUDING SUMMARY

Charge-exchange (p,n) reaction measurements with good energy resolution have been carried out on ^{59}Co in the energy range 90 MeV $\leq E_p \leq$ 200 MeV. We measuared excitation energies, cross sections, and subsequently calculated the GT strength distributions.

We found that the excitation energy of the IAS corresponds with previous measurements by other researchers and also confirmed predictions made that the first excited state would be the first GT transition.

This experminent has yielded the first detailed view of the dominant portion of the GT transition strengths for ^{59}Co. The GT strengths obtained at 120, 160, and 200 MeV were on average up to 69% of the value predicted by the model independent sum rule. This can be compared with a theoretical value, obtained by a Shell-Model calculation, of about 61%. At 90 MeV about 48% of the predicted value was observed. The summed GT strength does not include the strength in the continuum region since it is difficult to disentangle from the background. The Shell-Model calculation that reproduced the profile of strength distribution

of the GTGR predicts that no strength remains within the conventional Shell-Model space above 19 MeV.

The other strength that is predicted by the sum rule lies most probably in the continuum region. Various reasons, such as configuration mixing and Δ-hole excitations, have been given over the years why the undetected strength has shifted into the high excitation energy continuum. It is, however, not a straightfoward procedure to extract these strengths since the continuum is a collective excitation of both $L = 0$ transition as well as $L > 0$ transitions. To extract the strengths from these giant resonances, will require an additional project requiring multi decomposition of the cross sections.

The reason why the unit cross sections for odd-mass nuclei is larger than those for even-mass nuclei is still unsolved but this study has once again shown that the (p,n) reaction is an invaluable complement to weak-interaction decay studies. However, the way to proceed with this study lies with polarization transfer measurements since these provides a direct measure of the relative Gamow-Teller contribution in the isobaric analogue state, subsequently giving us a much better understanding of the nuclear structure.

Bibliography

[And62]   J.D.Anderson, C.Wong, and J.W.McClure, Isobaric states in nonmirror nuclei, Phys. Rev. 126, (1962) 217

[And65]   J.D.Anderson, C.Wong and J.W.McClure, Phys. Rev. 138B, (1965) 615

[Ari84]   A.Arima, Spin excitation in nuclei., Plenum Press, New York, (1984) 7

[Arnd83]   R.A.Arndt *etal.*, Phys. Rev. D, 28, (1983) 97

[Bohr69]   A.Bohr and Mottelson, Nucl. Struc. (Benjamin, New York, 1969), Vol.1, pp345, 349, 411

[Bopp86]   P. Bopp *et al.*, Phys. Rev. lett. 56, (1986) 919

[Bot86a]   A.H.Botha, H.N.Jungwirth, J.J.Kritzinger, Z.B.Du Toit, D.Reitmann, and S.Scheider, Proc. 11th Intern. Conf. on Cyclotrons and their Applications, Tokyo (1986) 9

[Bot86b]   A.H.Botha, S.J.Burger, Z.B.Du Toit, D.Reitmann, P.J.Cilliers, P.M.Cronje and H.N.Jungwirth, Proc. 11th Intern. Conf. on Cyclotrons and their Applications, Tokyo (1986) 515

[Bre87]   T.Bressani and G.Pauli, Hadronic Physics at Intermediate Energy,II, (1987) 351

[Bro88]   B.A.Brown, W.A.Richter, R.E.Julies,H.B.Wildenthal, Ann. Phys. 182, (1988) 191

[Bugg80]   D.V.Bugg *etal.*, Phys. Rev. C, 21, (1980) 1004

[Chi80]   H.C.Chiang and J.Hufner, Nucl. Phys. A349, (1980) 466

[Com82]   J.R.Comfort *et al.*, Phys. Rev. C, 26, (1982) 1800

[Firk79]   F.W.K.Firk, Nuclear Instruments and Methods 162, (1979) 539

[Gaa84]   C.Gaarde, J.Larsen, and J.Rappaport, Spin excitation in nuclei., Plenum Press, New York, (1984) 65

[Good80]   C.D.Goodman *et al.*, Phys. Rev. Lett. 44, (1980) 1755

[Gov72]   N.B.Gove and A.H.Wapstra, Nuclear Data Tables, Vol.II, no.2/3, 127 (1972)

[Hua91]   W.Huang, Polarization Transfer Measurements in the $^{19}F(\vec{p},\vec{n})^{19}Ne$ and $^{39}K(\vec{p},\vec{n})^{39}Ca$ Reactions at 120 and 160 MeV, Ph.D thesis, Indiana University, 1991

[Ikeda64] K.M.Ikeda, Prog. Theor. Phys. 31, (1964) 414

[Kab90]   R.Kabutz, B.Sc.(Hons.) project, University of Cape Town, 1990

[Kab92]   R.Kabutz, Private Communications, University of Cape Town, 1992

[Kle85]   A.Klein, W.G.Love, and N.Auerbach, Phys. Rev. C, 31, (1985) 710

[Kra88]   K.S.Krane, Introductory Nuclear Physics, (1988) 226

[Lan68]   A.Langsford, P.H.Bowen and G.C.Cox, Nucl. Phys. A113, (1969) 443

[Love81]   W.G.Love and M.A.Franey, Phys. Rev. C24, (1981) 1073

[Love85] W.G.Love and M.A.Franey, Phys. Rev. C31, (1985) 488

[Love87] W.G.Love *etal.*, Can. Jour. of Phys., 65, (1987) 536

[Mad89] R.Madey, B.S.Flanders, B.D.Anderson, A.R.Baldwin, J.W.Watson, S.M.Austin, C.C.Foster, H.V.Klapdor and K.Grotz, Phys. Rev. C 40, (1989) 540

[Mos82] J.M.Moss *et al.*, Phys. Rev. Lett. 48, (1982) 466

[NAC87] NAC Annual Report, June 1987

[NAC90] NAC Annual Report, June 1990

[New91] R.T.Newman, The Neutron Detection Efficiency of a Time-of-Flight Spectrometer, M.Sc thesis, University of Cape Town, 1991

[Petr69] F. Petrovich *et al.*, Phys. Rev. Lett. 22, (1969) 895

[Petr80] F.Petrovich, W.G.Love and R.J.McCarthy, Phys. Rev. C21, (1980) 1718

[Rap83] J.Rappaport, AIP Conf. Proc. 97, (1983) 365

[Satch64] G.R.Satchler, Nucl. Phys. 55, (1964) 1

[Tadd81] T.N.Taddeucci *etal.*, Phys. Rev. C, 25, (1981) 1094

[Tadd87] T.N.Taddeucci *et al.*, Nucl. Phys. A469, (1987) 125

[Tay69] B.N.Taylor, W.H.Parker and D.N.Langeberg, Rev. Mod. Phys. 28, (1969) 375

[Tep70] J.W.Tepel, J.G.Malan and J.A.M.de Villiers, Nucl. Phys. A128, (1970) 129

[Van92] M.G.Van der Merwe, The Effective Interaction in Large Model Spaces, Ph.D thesis, University of Stellenbosch, 1992

[Wei83] W.Weise, Nucl. Phys. A396, (1983) 373

[Wilk82] Nucl. Phys. A377, (1982) 474

[Wong90] Samuel S.M. Wong, Intr. Nucl. Phys, (1990) 225